IOP Publishing Semiconductor Science and Technology
Semicond. Sci. Technol. 31 (2016) 083002 (22pp) doi:10.1088/0268-1242/31/8/083002

Topical Review

Review on first-principles study of defect properties of CdTe as a solar cell absorber

Ji-Hui Yang[1], Wan-Jian Yin[1,2], Ji-Sang Park[1], Jie Ma[3] and Su-Huai Wei[4]

[1] National Renewable Energy Laboratory, Golden, CO 80401, USA
[2] College of Physics, Optoelectronics and Energy & Collaborative, Innovation Center of Suzhou Nano Science and Technology, Soochow University, Suzhou 215006, People's Republic of China
[3] Lawrence Berkeley National Laboratory, Berkeley 94720, USA
[4] Beijing Computational Science Research Center, Beijing 100094, People's Republic of China

E-mail: suhuaiwei@csrc.ac.cn

Received 4 May 2015, revised 23 May 2016
Accepted for publication 27 May 2016
Published 15 July 2016

Abstract

CdTe is one of the leading materials for high-efficiency, low-cost, and thin-film solar cells. In this work, we review the recent first-principles study of defect properties of CdTe and present that: (1) When only intrinsic defects are present, *p*-type doping in CdTe is weak and the hole density is low due to the relatively deep acceptor levels of Cd vacancy. (2) When only intrinsic defects present, the dominant non-radiative recombination center in *p*-type CdTe is Te_{Cd}^{2+}, which limits the carrier lifetime to be around 200 ns. (3) Extrinsic *p*-type doping in CdTe by replacing Te with group V elements generally will be limited by the formation of AX centers. This could be overcome through a non-equilibrium cooling process and the hole density can achieve 10^{17} cm^{-3}. However, the long-term stability will be a challenging issue. (4) Extrinsic *p*-type doping by replacing Cd with alkaline group I elements is limited by alkaline interstitials and a non-equilibrium cooling process can efficiently enhance the hole density to the order of 10^{17} cm^{-3}. (5) Cu and Cl treatments are discussed. In bulk CdTe, Cu can enhance *p*-type doping, but Cl is found to be unsuitable for this. Both Cu and Cl show segregation at grain boundaries, especially at those with Te–Te wrong bonds. (6) External impurities are usually incorporated by diffusion. Therefore, the diffusion processes in CdTe are investigated. We find that cation interstitial (Na_i, Cu_i) diffusion follows relatively simple diffusion paths, but anion diffusion (Cl_i, P_i) follows more complicated paths due to the degenerated defect wavefunctions.

Keywords: defect control, CdTe, solar cell

(Some figures may appear in colour only in the online journal)

1. Introduction

Cadmium Telluride (CdTe) has been studied for more than half a century as a promising material for high-efficiency, low-cost, and thin-film solar cell applications [1, 2]. It has a direct band gap of ~1.45 eV, which is optimally matched to the solar spectrum for photovoltaic (PV) energy conversion. It also has a large optical absorption coefficient of $>5 \times 10^5$ cm^{-1}, allowing it to absorb most of the sunlight with a very thin layer of about 2 μm thickness. Furthermore, CdTe is a rare II–VI semiconductor that can be doped relatively easily for both *n*-type and *p*-type, making it an attractive material for optoelectronic devices such as photodiodes and optical detectors as well as solar cells. Despite this, CdTe solar cells based on homo *p-n* junctions usually have low energy conversion efficiency due to the large surface recombination caused by the high surface-to-volume ratio in very thin (~2 μm) CdTe absorbers [3]. As a result, most of the present high-efficiency CdTe solar cells adopt an architecture shown in figure 1, which comprises a heterojunction of a

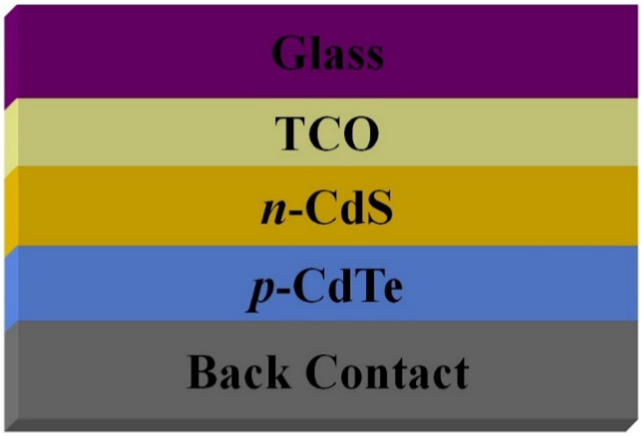

Figure 1. Diagram to show the common architecture of a high-efficiency CdTe solar cell.

p-type CdTe absorber layer and an *n*-type CdS window layer with a CdTe surface buried into the CdS. Much effort has been devoted to understanding CdTe/CdS heterojunctions and improving CdTe solar cell efficiency in recent decades [3–15]. With the development of techniques for doping controls, material growth, and device optimization, the energy conversion efficiency of CdTe solar cells has steadily been improved and recently First Solar has achieved a record cell efficiency of 22.1% [16]. However, this efficiency still lacks theoretical maximum efficiency (~30%).

Macroscopically, the efficiency of a solar cell device can be evaluated by the maximum output power divided by the input power of the incident sunlight. The maximum output power, on the other hand, depends on (actually is the product of) three factors: open circuit voltage (V_{oc}), short circuit current (J_{sc}), and filling factor (*FF*). Consequently, the solar cell efficiency is determined by these three factors when the incident sunlight is certain. Microscopically, V_{oc}, J_{sc} and *FF* are related to carrier density and carrier lifetime. Typically, large carrier density can lead to large Fermi level splitting and thus large V_{oc} (as explained below) and long carrier lifetime can result in large J_{sc} and *FF* as well as large V_{oc} [17, 18]. Hence, to achieve high efficiency for a solar cell, these quantities, including V_{oc}, carrier density, and carrier lifetime, must be optimized. For *p*-type CdTe-based solar cells, the typical values of V_{oc}, hole density, and carrier lifetime are: 850 meV, 10^{14} cm^{-3}–10^{15} cm^{-3}, and a few *ns*, respectively. Compared to the band gap of CdTe and other high-efficiency solar cells with similar band gaps such as GaAs [17], the V_{oc} of a CdTe solar cell is relatively low, hole density is relatively small, and carrier lifetime is too short. These three issues are thus among the key factors hindering the current progress of CdTe solar cell technology. Only if they are fully understood and resolved, can the efficiency of *p*-type CdTe-based solar cells be further increased. Besides the efficiency issue, another key issue in CdTe solar cells is performance stability, i.e. how long a CdTe solar cell can keep working before its efficiency decays too much. This question is important for the broad application of CdTe technology.

Basically, both the efficiency and stability issues are related to the defect properties of CdTe. For example, defects can determine doping levels and thus carrier density, which is related to V_{oc}, i.e. high V_{oc} often requires high carrier density [19]; defects with deep in-gap levels can cause non-radiative recombination, which often dominates carrier lifetime and thus V_{oc}, J_{sc} and *FF* [17, 18], i.e. usually, the longer the carrier lifetime, the larger the V_{oc}, J_{sc} and *FF*; defects can move/diffuse in CdTe and change its electronic properties, which can cause device performance degradation [12, 20–22]. Due to the important role defects play in determining the efficiency and stability of CdTe solar cells, knowledge of defect properties in CdTe, including both intrinsic and extrinsic defects, is thus strongly desired. Both experiments and theories have contributed significantly to understanding defect behaviors in CdTe during recent decades [19–49], with the aim mainly focused on the following aspects: what are the main intrinsic defects in CdTe that introduce or limit carrier density; what is the dominant defect that causes the electron–hole recombination in CdTe, thus limiting its carrier lifetime; can group V element doping increase hole density; what roles do Cu and Cl play in polycrystalline CdTe; how and how fast do dopants diffuse in CdTe?

With the help of first-principles calculation methods, here we review the recent first-principles study of defect properties of CdTe, mainly using our theoretical calculation results [50–57]. Available experimental and theoretical works are also provided and discussed [19–49]. Our review is organized as follows. In section 2, we will describe the calculation methods used in our work. In section 3, we will discuss the intrinsic defect properties of CdTe, deduce its achievable V_{oc} with the help of quantitative thermodynamic simulation, and study in detail the non-radiative recombination processes in CdTe. In section 4, we will discuss *p*-type doping of CdTe using extrinsic dopants including group-VA and group-IA elements and explore whether high hole density can be achieved. Potential performance stability issues will also be discussed. In section 5, we will focus on the discussion of Cu and Cl defect behaviors in the bulk and grain-boundary (GB) regions of CdTe. In section 6, we will investigate impurity diffusion in CdTe, which can help us to understand dopant incorporation and the stability problem. Finally, we will summarize the works related to defects in CdTe and briefly discuss the remaining defect problems and possible directions to further improve CdTe solar cells.

2. Calculation methods

2.1. First-principles calculations of defect properties

Our first-principles calculations were performed using density-functional theory (DFT) [58, 59] as implemented in the VASP code [60, 61]. The electron and core interactions are included, using the frozen-core projected augmented wave (PAW) approach [62]. To correct the band-gap error, we used the Heyd–Scuseria–Ernzerhof (HSE06) hybrid functional [63]. Our calculated lattice constant of pure CdTe is 6.58 Å

with a band gap of 1.49 eV, in good agreement with the experiments. For all the HSE06 supercell calculations, all the atoms are fully relaxed until the forces on every atom are less than 0.05 eVÅ^{-1}. For GBs, calculations are performed using the generalized gradient approximation (GGA) formulated by Perdew, Burke, and Ernzerhof (PBE) [64] due to large system sizes.

To determine the defect formation energies and defect transition energy levels, we calculated the total energy $E(\alpha, q)$ for a CdTe supercell containing the relaxed defect α in its charge state q. We also calculated the total energy E(CdTe) for the same supercell in the absence of the defect, as well as the total energies of elemental solids or gases at their stable phases. The defect formation energy $\Delta H_f(\alpha, q)$ as a function of the electron Fermi level E_F and the atomic chemical potentials μ_i is given by [65]:

$$\Delta H_f(\alpha, q) = \Delta E(\alpha, q) + \sum n_i \mu_i + qE_F, \quad (1)$$

where $\Delta E(\alpha, q) = E(\alpha, q) - E(\text{CdTe}) + n_i E(i) + qE_{\text{VBM}}$, E_F is referenced to the valence band maximum (VBM) of bulk CdTe, and μ_i is the chemical potential of constituent i referenced to elemental solid or gas with energy $E(i)$. The n's are the numbers of atoms taken out of the supercell to form the defects, and q is the number of electrons transferred from the supercell to the Fermi reservoirs to form the defect cell. The defect transition energy level $\varepsilon_\alpha(q/q')$ is the Fermi level E_F in equation (2) at which the formation energy $\Delta H_f(\alpha, q)$ of defect α at charge q is equal to that of the same defect at another charge state q', i.e.

$$\varepsilon_\alpha(q/q') = [\Delta E(\alpha, q) - \Delta E(\alpha, q')]/(q' - q). \quad (2)$$

To get fast convergence on total energy and transition energy levels and good descriptions on the symmetry of the defect state, we used a mixed scheme [65, 66] to determine $\varepsilon_\alpha(q/q')$. In this scheme, for an acceptor ($q < 0$), the ionization energy level with respect to the VBM is given by

$$\begin{aligned}\varepsilon(0/q) &= [\varepsilon_D^\Gamma(0) - \varepsilon_{\text{VBM}}^\Gamma(\text{host})] \\ &\quad + \{E(\alpha, q) - [E(\alpha, 0) \\ &\quad - q\varepsilon_D^k(0)]\}/(-q).\end{aligned} \quad (3)$$

For donor levels ($q > 0$), the ionization energy referenced to the conduction band minimum (CBM) is given by

$$\begin{aligned}\varepsilon_g^\Gamma(\text{host}) - \varepsilon(0/q) &= [\varepsilon_{\text{CBM}}^\Gamma(\text{host}) - \varepsilon_D^\Gamma(0)] \\ &\quad + \{E(\alpha, q) - [E(\alpha, 0) - q\varepsilon_k^D(0)]\}/q\end{aligned} \quad (4)$$

where $\varepsilon_k^D(0)$ and $\varepsilon_D^\Gamma(0)$ are the defect levels at the special k points (averaged) and at the Γ point, respectively; $\varepsilon_{\text{VBM}}^\Gamma(\text{host})$ and $\varepsilon_{\text{CBM}}^\Gamma(\text{host})$ are the VBM and CBM energy, respectively, of the pure CdTe supercell at the Γ point. The first term on the right-hand side of equations (4) or (5) gives the single-electron defect level at the Γ point (note that only referenced to some level, i.e. the VBM of the host, can the defect level be meaningful). The second term determines the relaxation energy parameter U (including both the Coulomb contribution and atomic relaxation contribution) of the charged defect calculated at the special k points, which is the extra cost of energy after moving ($-q$) charge to the neutral defect level with $E = \varepsilon_k^D(0)$. Note that, if single Γ point is used, we will have $\varepsilon_k^D(0) = \varepsilon_D^\Gamma(0)$ and equations (4) or (5) will be exactly the same as equation (2). However, because usually small supercells are used for defect calculations in reality, special k points with dense meshes are necessary to give accurate total energies and charge densities, but single Γ point cannot. In this case, the additional electrons or holes needed to form the charged defects are also added to these special k points with energy cost $\varepsilon_k^D(0)$, which is usually different from $\varepsilon_D^\Gamma(0)$. This difference is also known as the band-filling correction, which is naturally included in the mixed scheme [67]. Once we know the defect transition energy levels, the formation energy of a charged defect is then given by

$$\Delta H_f(\alpha, q) = \Delta H_f(\alpha, 0) - q\varepsilon(0/q) + qE_F, \quad (5)$$

where $\Delta H_f(\alpha, 0)$ is the formation energy of the charge-neutral defect and E_F is the Fermi level with respect to the VBM. To evaluate the effect of image interaction of charged defects and supercell size, we carefully check the transition energy levels in 512-atom supercells and find that the defect transition energy levels are converged to within 0.1 eV.

2.2. Thermodynamic simulation methods

Under thermodynamic equilibrium growth conditions and within the dilute limit, the density of a defect α with charge state q is a function of Fermi level and can be calculated as

$$n(\alpha, q) = N_{\text{site}} g_q e^{-\Delta H_f(\alpha, q)/k_B T}, \quad (6)$$

where, N_{site} is the number of possible sites per volume for defect α, g_q is the degeneracy factor related to possible electron occupations [68, 69], and $\Delta H_f(\alpha, q)$ is the formation energy of a defect α at charge state q, as shown in equations (1) or (5). At a given temperature, the thermally excited electron density n_0 and hole density p_0 are also functions of Fermi level, which are given as

$$\begin{aligned}n_0 &= N_c e^{-\frac{E_c - E_F}{k_B T}}, \; N_c = 2\frac{(2\pi m_n^* k_B T)^{\frac{3}{2}}}{h^3}, \\ p_0 &= N_v e^{-\frac{E_F - E_v}{k_B T}}, \; N_v = 2\frac{(2\pi m_p^* k_B T)^{3/2}}{h^3}.\end{aligned} \quad (7)$$

Here, N_c is the temperature-dependent effective density of states of the conduction band that can accept electrons and N_v is the effective density of states of the valence band that can accept holes. m_n^* (0.095 m_0 for CdTe) and m_p^* (0.84 m_0 for CdTe) are effective masses of electrons and holes, taking into account the spin degeneracy and spin–orbital coupling [69, 70]. The neutralization condition in a semiconductor system with defects requires that

$$p_0 + \sum_i q_i n_{D_i}^{q_i+} = n_0 + \sum_j q_j n_{A_j}^{q_j-}, \quad (8)$$

where $n_{D_i}^{q_i+}$ is the density of a donor D_i with charge state q_i and $n_{A_j}^{q_j-}$ is the density of an acceptor A_j with charge state $-q_j$. By solving equations in (1) and (6)–(8) self-consistently, we can obtain the E_F of a semiconductor system at given chemical potentials, as well as carrier densities and defect

densities, when this material is grown under equilibrium conditions at a given growth temperature.

When rapidly cooling to a low temperature (e.g. room temperature), the total density of a defect α generated at a high temperature, which is the sum of densities of α with all possible charge states, is assumed to be unchanged. This approximation, known as freezing-in approximation [38], is reasonable in the case where defects have barriers large enough to be immobile at low temperatures. Under this approximation, the only possible change after the rapid cooling is the redistribution of defect densities at different charge states according to their weights. For example, considering a defect α with two charge states 0 and q, the density of α with charge state q is recalculated as [53, 57]

$$n'(\alpha, q) = N_\alpha \times \frac{g_q e^{-\Delta H_f(\alpha,q)/k_B T}}{g_q e^{-\Delta H_f(\alpha,q)/k_B T} + g_0 e^{-\Delta H_f(\alpha,0)/k_B T}}, \quad (9)$$

where N_α is fixed as the total number of defect α at growth temperature, $g_q e^{-\Delta H_f(\alpha,q)/k_B T}$ and $g_0 e^{-\Delta H_f(\alpha,0)/k_B T}$ are the weights of defect α at charge q and charge-neutral states, respectively. By solving the equations in (6)–(9) self-consistently, we can get a new set of E_F, carrier densities, and defect densities with different charge states after the sample is quenched.

2.3. Electron–phonon coupling calculation methods

The electron–phonon coupling parts are calculated following the method described in [71, 72] based on static approximations [73, 74]. The non-radiative decay probability between the initial electronic state i and the final electronic state j is given by the conventional Fermi 'golden rule' expression

$$W_{ij} = \frac{2\pi}{\hbar} \sum_n \sum_m p(i, n) |V_{in,jm}|^2 \delta(E_{in} - E_{jm}), \quad (10)$$

where $V_{in,jm}$ are the off-diagonal matrix elements of the total Hamiltonian defined as $V_{in,jm} = \langle \Psi_{j,m}(r, R) | H | \Psi_{i,n}(r, R) \rangle$, and $p(i, n)$ is the probability that the system is in the initial state $\Psi_{i,n}(r, R)$, so that $\sum_n p(i, n) = 1$. Provided that the vibrational equilibrium rate considerably exceeds the non-radiative decay rate, $p(i, n)$ can be described by Boltzmann distribution

$$p(i, n) = Z^{-1} \exp(-\beta E_{in}), \quad (11)$$

where $Z = \sum_n \exp(-\beta E_{in})$ is the partition function and $\beta = (k_B T)^{-1}$. Under static approximations [73, 74], $V_{in,jm}$ can be written as

$$\begin{aligned}
&\langle \Psi_{j,m}(r, R) | H | \Psi_{i,n}(r, R) \rangle \\
&= \langle \psi_j(r, R_a) \varphi_{j,m}(R) | H_a + \sum_k \frac{\partial H}{\partial Q_k} (Q_k - Q_{k,a}) \\
&\quad \times | \psi_i(r, R_a) \varphi_{i,n}(R) \rangle \\
&= \sum_k \langle \psi_j(r, R_a) | \frac{\partial H}{\partial Q_k} | \psi_i(r, R_a) \rangle \langle \varphi_{i,n}(R) | \\
&\quad \times (Q_k - Q_{k,a}) | \varphi_{j,m}(R) \rangle \\
&= \sum_k C_{i,j}^k \cdot \langle \varphi_{i,n}(R) | \boldsymbol{Q_k} | \varphi_{j,m}(R) \rangle. \quad (12)
\end{aligned}$$

Here, R_a is the relaxed atomic position of state i or j and $Q_{k,a}$ is normal phonon mode of electronic state i or j. By definition, $\boldsymbol{Q_k} \equiv Q_k - Q_{k,a}$, is atomic vibration for the phonon state k, which can be calculated for electronic state i and j as

$$\boldsymbol{Q_{(i,j)k}} = \frac{1}{\sqrt{M_k}} \sum_R M_R \mu_k(R) \boldsymbol{R_{i,j}}. \quad (13)$$

Here, $\mu_k(R)$ is the kth phonon mode vector, and M_R is the nuclear mass for atom R. Under harmonic approximation, the phonon modes for electronic state i and j are the same and we have

$$\boldsymbol{Q_j} = \boldsymbol{Q_i} + \boldsymbol{K}, \quad (14)$$

where $\boldsymbol{K_k} = \frac{1}{\sqrt{M_k}} \sum_R M_R \mu_k(R) \Delta \boldsymbol{R_{j,i}}$. Here $\Delta \boldsymbol{R_{j,i}} = \boldsymbol{R_j}(0) - \boldsymbol{R_i}(0)$ is the relaxed atomic position difference of the system at the electronic states i and j. Then, the electron–phonon coupling constant between electronic states i and j and phonon mode k is

$$\begin{aligned}
C_{i,j}^k &= \langle \psi_j(r, R_a) | \frac{\partial H}{\partial Q_k} | \psi_i(r, R_a) \rangle \\
&= \sum_R \mu_k(R) \langle \psi_j | \frac{\partial H}{\partial R} | \psi_i \rangle. \quad (15)
\end{aligned}$$

And the phonon modes satisfy

$$\sum_R M_R \mu_k(R) \mu_l(R) = \delta_{k,l}. \quad (16)$$

We calculated all the zone-centered phonon modes using density-functional perturbation theory as implemented in VASP. For the term $\langle \psi_j | \frac{\partial H}{\partial R} | \psi_i \rangle$, we used the recently proposed variational method [71, 72]. For a local/semilocal exchange-correlation functional, the Kohn–Sham Hamiltonian is written as

$$H_R = -\frac{1}{2}\nabla^2 + \sum_{l,R} |\varphi_{l,R}\rangle \langle \varphi_{l,R}| + V_{\text{tot}}(r, R), \quad (17)$$

and here $\varphi_{l,R}$ is the nonlocal potential projector for atom R and angular momentum l. Thus,

$$\begin{aligned}
&\langle \psi_j(r) | \frac{\partial H}{\partial R} | \psi_i(r) \rangle \\
&= \sum_l \langle \psi_j(r) | \left[|\varphi_{l,R}\rangle \left\langle \frac{\partial \varphi_{l,R}}{\partial R} \right| + \left| \frac{\partial \varphi_{l,R}}{\partial R} \right\rangle \langle \varphi_{l,R}| \right] | \psi_i(r) \rangle \\
&\quad + \int \psi_j(r) \psi_i(r) \frac{\partial}{\partial R} V_{\text{tot}}(r, R) \mathrm{d}^3 r. \quad (18)
\end{aligned}$$

The first term is the same as in Hellman–Feynman force evaluation, which can readily be calculated. For the second term, $\rho_\lambda(r) = \sum_{i' \in occ} |\psi_{i'}(r)|^2 + \lambda \psi_j(r) \psi_i(r)$ and it can be shown that $\int \psi_j(r) \psi_i(r) \frac{\partial}{\partial R} V_{\text{tot}}(r, R) \mathrm{d}^3 r = \frac{\mathrm{d}}{\mathrm{d}R} F_R$ [71], with F_R being the *ab initio* atomic force on atom R calculated from the Hellman–Feynman formula, while keeping $\rho_\lambda(r)$ fixed during self consistent field (SCF) iterations. This part is calculated using the PEtot code [71, 72]. After we obtain the

non-radiative decay probability W_{ij}, the capture rate constant is $B = W_{ij} \cdot V$, where V is the volume of the supercell.

2.4. Energy barrier and transition rate calculation methods

We calculated the related energy barriers using the HSE06 hybrid functionals ($\alpha = 0.25$) and nudged elastic band (NEB) method [75] as implemented in VASP code unless stated otherwise. Five images are used. After the local minimum and transition state are obtained, the transition rate ν for a defect or particle to overcome its barrier is defined as [76]

$$\nu = \frac{\prod_{i=1}^{3N-3} \omega_i}{\prod_{i=1}^{3N-4} \omega_j}, \tag{19}$$

where ω_i are $3N - 3$ positive phonon frequencies at the local minimum configuration and ω_j are $3N - 4$ positive phonon frequencies at the saddle-point. At this step, the zone-centered phonon frequencies at the minimum and saddle-point are calculated within the PBE framework by making finite displacements (0.015 Å) and we fixed the atoms, which are more than 5 Å away from the defect centers.

3. Intrinsic defects in bulk CdTe

3.1. Defect properties of intrinsic CdTe

Intrinsic defects of CdTe have been extensively studied and the characteristics of some defects are still under debate from both theoretical and experimental points of view. The first important intrinsic defect is the Cd vacancy, which can have 0, −1 and −2 states (see figure 5). For charge-neutral Cd vacancy, while some works reported the Jahn–Teller structure distortion, which makes Cd vacancy most stable at the D_{2d} state [36, 44], other works [32–35, 41–43] did not report this effect. For the −1 state of Cd vacancy, the Jahn–Teller distorted C_{3v} state is reported most stable in references [44] and [45], while other works did not find this. Cd vacancy with the −2 state is congruously found most stable at the T_d state. The defect transition energy levels of Cd vacancy are also rather diverse, both experimentally and theoretically, ranging from 0.1–0.8 eV above the VBM of CdTe [31–36, 41–49]. The second important intrinsic defect is Te vacancy. Some works reported Jahn–Teller structure distortion for neutral V_{Te} [35, 41] and some did not [32, 33, 42, 43]. Most of these works, however, found Te vacancy transition energy levels deep in the band gap of CdTe. For other defects, Te_{Cd} antisite is found to have Jahn–Teller distortion (see figure 4) at its neutral state in most recent works [35, 36, 41, 44], which is different from earlier work [33]. Te interstitial is reported to be most stable at a splitting site [35, 41] acting as a donor, while earlier work found Te interstitial at the tetragonal site acting as an acceptor [33].

Figure 2 shows our recent HSE06 calculated results for the intrinsic defect formation energies as a function of E_F under Cd-rich and Te-rich growth conditions. Compared to the results reported in most of the previous works, our HSE06 results mainly show two different characteristics. First, the

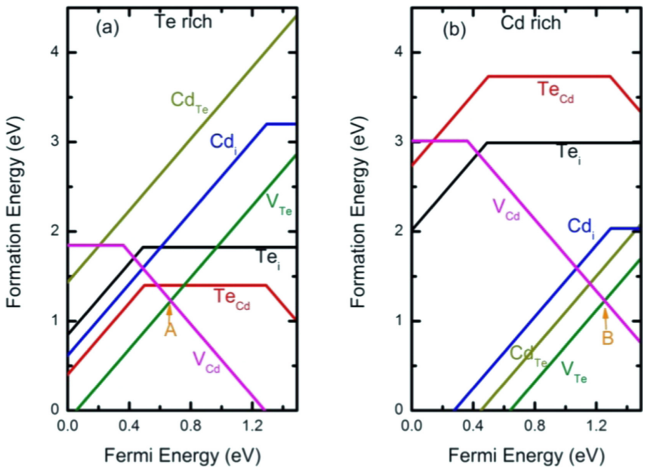

Figure 2. Intrinsic defect formation energies versus E_F in CdTe under (a) Te-rich condition and (b) Cd-rich condition.

(0/2−) transition energy level of Cd vacancy is 0.36 eV above the VBM and the (0/−) level is found even deeper in the band gap with a value of 0.85 eV above the VBM (see figure 5). This is different from all previous works. The relatively deep acceptor levels can be understood by the large local Jahn–Teller structure distortion around V_{Cd} at its charge-neutral state, where two Te atoms get closer and the other two Te atoms get more separated, thus splitting the original three-fold-degenerated defect states (without spin–orbit coupling) with T_d symmetry to D_{2d} symmetry with two degenerated fully occupied states and one unoccupied state, which lies above the CBM [53]. Our structure results are consistent with those found in [36, 44]. Due to the upshift of this unoccupied state, it costs more energy for neutral V_{Cd} to accept electrons from the VBM, leading to its relatively deep transition levels. Another characteristic, which is also different from all previous works, is that V_{Te} is now a rather shallow and dominant donor with its (2+/0) transition energy level above the CBM, although both our study and those in [35, 41] found that neutral V_{Te} is most stable at a Jahn–Teller distorted state, where two Cd atoms form a bond and the other two Cd atoms are far separated [50]. The rather shallow donor level might result from the HSE06 functional strengthening the correlation interactions of the defect states, which lift the neutral point defect level up.

To get more accurate defect information of intrinsic CdTe, we performed thermodynamic simulation by considering all the defects in figure 2 under equilibrium growth conditions (left panels in figure 3) and after rapid cooling (right panels in figure 3). The obtained Fermi level positions, carrier densities, and defect densities as functions of growth conditions (chemical potentials and temperatures) are shown in figure 3. We see that under equilibrium growth conditions, as the growth temperature increases, more defects can be created and the E_F is pushed down for p-type doping (under Te-rich condition) or up for n-type doping (under Cd-rich condition), enlarging the variation range of E_F. However, no matter how high the growth temperature is, the E_F will be

pinned around 0.7 eV or near position A in figure 2(a) for *p*-type doping, which is the lowest E_F achievable for *p*-type CdTe under thermodynamic equilibrium growth conditions. This is because if E_F is lower than A, the formation energy of V_{Te}^{2+} would be lower than that of V_{Cd}^{2-}, thus more V_{Te}^{2+} would form than V_{Cd}^{2-}, pushing the E_F up. Similarly, for *n*-type doping, the Fermi level will be pinned around 1.3 eV or position B in figure 2(b), which is the highest Fermi level for *n*-type CdTe under equilibrium growth conditions. As a result of this intrinsic self-doping limit, the largest possible Fermi level splitting of intrinsic CdTe solar cells grown under equilibrium conditions will be limited by the difference between the two pinning points A and B, which is only about 0.6 eV.

However, things can be well improved after rapid cooling. From equation (7), we see that if we maintain high hole density when the temperature is reduced, the Fermi level can be lowered toward the VBM, or if we maintain high electron density when the temperature is reduced, the Fermi level can be raised toward the CBM. As discussed above, we can achieve high carrier density if we grow the sample at a high temperature. Note that the carrier densities are actually determined by the density differences between the acceptors and donors. Under the freezing-in approximation [38] during the rapid-cooling process, once defects are formed at high temperatures, their densities can be kept after the temperature is reduced. Consequently, high carrier density can also be kept, except that the defect ionization might get weaker due to the temperature reduction and the carrier density might decrease slightly. As a result, the rapid-cooling strategy can effectively improve the doping efficiency and is commonly used in the experimental doping process.

The right panels of figure 3 show the Fermi levels, carrier densities and defect densities as functions of the Cd chemical potential after rapid cooling in CdTe. The hole density for *p*-type CdTe after rapid cooling from high temperature growth (such as $T = 800$ and 1200 K) is in the order of 10^{14} cm^{-3}, which agrees well with experiments [81]. Notably, for *p*-type CdTe grown under Te-rich condition, the Fermi level is lowered after rapid cooling, while for *n*-type CdTe under Cd-rich condition, the Fermi level is raised. Our results are consistent with the previous work of Berding [32], in which Fermi level splitting in CdTe is also found to be enlarged after rapid cooling, although in her local density approximation (LDA) calculation, the band gap is severely underestimated. What is more important is that our calculations show that after rapid cooling from high growth temperatures, the Fermi levels can be tuned beyond the self-doping limit under equilibrium growth conditions. According to our calculations, if *p*-type CdTe is grown at 800 K at Te-rich condition, a Fermi level of 0.35 eV above the VBM can be obtained. Likewise, if *n*-type CdTe is grown at 1200 K under Cd-rich condition, a Fermi level of 1.42 eV can be achieved after rapid cooling. Therefore, a Fermi level splitting of 1.07 eV is, in principle, achievable by intrinsic doping alone in homo CdTe *p*-*n* junction, which could significantly improve the open circuit

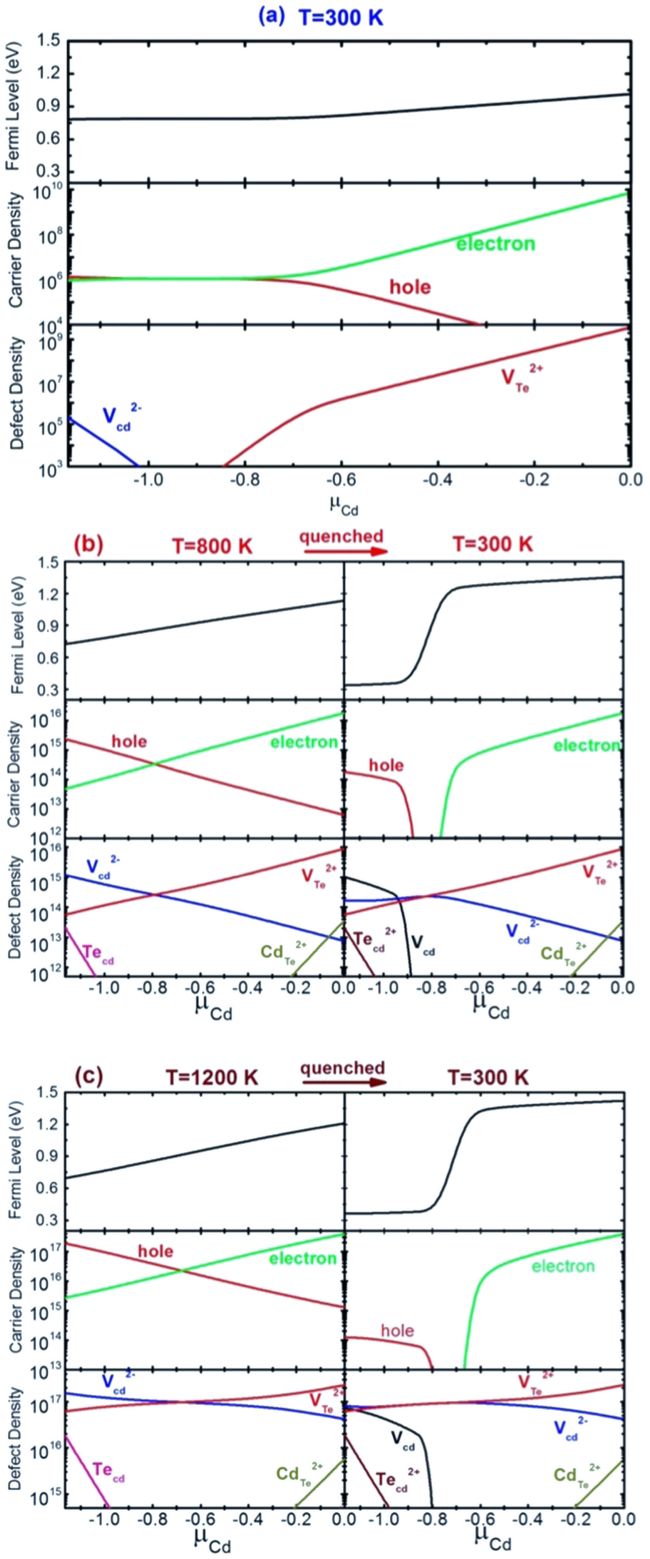

Figure 3. Fermi level, carrier density, and defect density as a function of Cd chemical potential under thermodynamic equilibrium growth conditions are shown in (a) at $T = 300$ K and the left panels of (b) at $T = 800$ K and (c) at $T = 1200$ K, respectively. The right panels of (b) and (c) show the quenched (to $T = 300$ K) Fermi level, carrier density, and defect density as a function of Cd chemical potential.

voltage of CdTe solar cells to be larger than their present typical value of 850 mV based on CdTe/CdS junction.

However, as we mentioned in the introduction, CdTe solar cells based on homo *p-n* junctions usually have large surface recombination caused by high surface-to-volume ratio in very thin (~2 μm) CdTe absorbers [3]. If the surface recombination problem can be suppressed, e.g. using MgCdTe or MnCdTe alloys to passivate the CdTe surface, it may be possible to achieve high-efficiency CdTe solar cells based on their homo *p-n* junctions. Right now, for CdTe solar cells based on *p*-CdTe/*n*-CdS heterojunctions, the critical issue is to improve the V_{oc} by pushing the *p*-type Fermi level as close to the VBM of CdTe as possible. However, in this case, our simulations show that for intrinsic CdTe, the *p*-type Fermi level will always be limited by the relatively deep V_{Cd} acceptor level and the hole density is always limited below $\sim 10^{15}$ cm^{-3}, no matter at what growth temperature. To get a shallower *p*-type Fermi level and a higher hole density, extrinsic doping using dopants with shallower acceptor levels is desired.

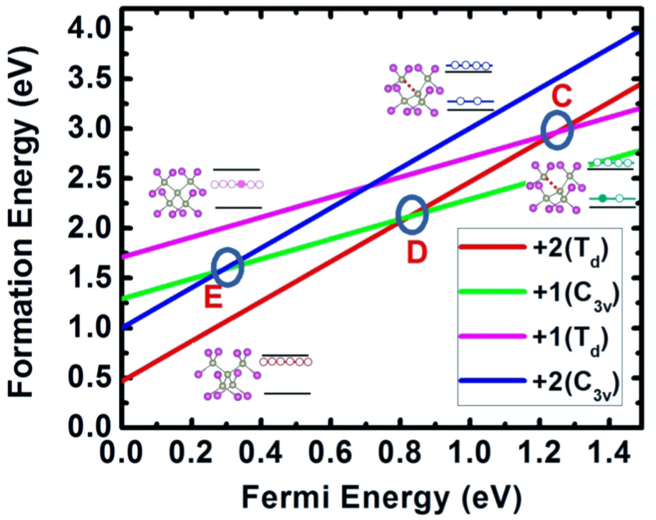

Figure 4. HSE06 calculated formation energies of Te on Cd antisite at the +2 and +1 charge states in *p*-type CdTe as functions of Fermi energies (referenced to the VBM). The inset shows the atomic and electronic configurations for different states. the pink balls are Cd and the light yellow balls are Te.

3.2. Non-radiative recombination in p-type CdTe

Non-radiative recombination can reduce solar cell efficiency by reducing the collection of photo-generated carriers and carrier lifetime. In a non-radiative recombination process, one electron (hole) is first trapped by defects through defect transition energy levels with the help of phonons and then one hole (electron) is trapped, leading to carrier recombination. Usually, direct experimental measurement of such processes is difficult [77–79]. As a result, quantitative calculations from first-principles would be very helpful. In the classical Shockley–Read–Hall (SRH) theory, the carrier capture rate U_c is the product of defect densities N_D, carrier densities n for electrons or p for holes, and carrier capture rate constant B, written as $U_{pc} = B_p p N_D$ for holes or $U_{nc} = B_n n N_D$ for electrons [80]. Consequently, the non-radiative recombination center candidates should have significant densities, i.e. the defect densities can be comparable to carrier densities.

In *p*-type CdTe doped by intrinsic defects, our thermodynamic simulations already show that if CdTe is grown at a typical temperature $T = 800$ K and quenched to room temperature under Te-rich condition, only four defects have significant densities: V_{Cd}, V_{Cd}^{2-}, Te_{Cd}^{2+}, and V_{Te}^{2+}, with densities of 1.03×10^{15}, 1.66×10^{14}, 2.15×10^{13}, and 5.56×10^{13} cm^{-3}, respectively, and the hole density is 1.77×10^{14} cm^{-3} with the Fermi level of 0.35 eV above the VBM. To be an effective recombination center, a defect should have a defect transition level close to the CBM when it traps an electron and have a defect level close to the VBM when it traps a hole. If only a single level is involved in both processes, it implies that the defect level should be close to the middle of the band gap, as the SRH model suggests. The probability of trapping more than one carrier is usually very small and such cases are not considered here. In considering these, we find that, the $(+2/+)$ transition energy level of V_{Te}^{2+} is above the CBM, and the $(-2/-)$ transition energy level of V_{Cd}^{2-} is below the VBM; therefore, both V_{Te}^{2+} and V_{Cd}^{2-} cannot be effective recombination centers and only Te_{Cd}^{2+} and V_{Cd} can be candidates as carrier recombination centers as shown in figures 4 and 5. Because these two defects can only trap electrons, the first step of the whole recombination process should be the electron-trapping process. Only after electron trapping is hole trapping meaningful.

By carefully considering the defect transition energy levels related to Te_{Cd}^{2+} and V_{Cd} during the trapping processes, we systematically identified that the non-radiative recombination caused by Te_{Cd}^{2+} and neutral V_{Cd} can involve their possible defect levels at points C, D, E in figure 4 and points F, G in figure 5 with defect energy levels of 1.24 , 0.82, 0.29, 0.85, and 0.22 eV above the VBM, respectively [56]. Considering the basic procedure that the electron is trapped first and then the hole can be trapped, we conclude that the dominant electron-trapping process can happen through defect levels at points C, D, and F, and the dominant hole-trapping process can happen through defect levels at points D, E, F, and G. Other processes are not important and are thus neglected.

Using the newly developed theoretical calculation methods for carrier capture rate through multi-phonon emissions (MPE) by Shi *et al* [71, 72] and with static approximations [73, 74], we have calculated the carrier capture rate constants through the above-mentioned levels for holes and electrons, as shown in table 1. For each process, we used the phonon modes and electron–phonon coupling constants based on the initial states as an approximation within the harmonic phonon approximation. Considering the whole recombination process can only start from electron trapping due to Te_{Cd}^{2+} and neutral V_{Cd}, we can exclude neutral V_{Cd} as dominant recombination centers, because electron trapping through defect level at point F is very slow with an electron capture rate constant of 3.54×10^{-10} cm^3 s^{-1}. For Te_{Cd}^{2+}, if electrons and holes are

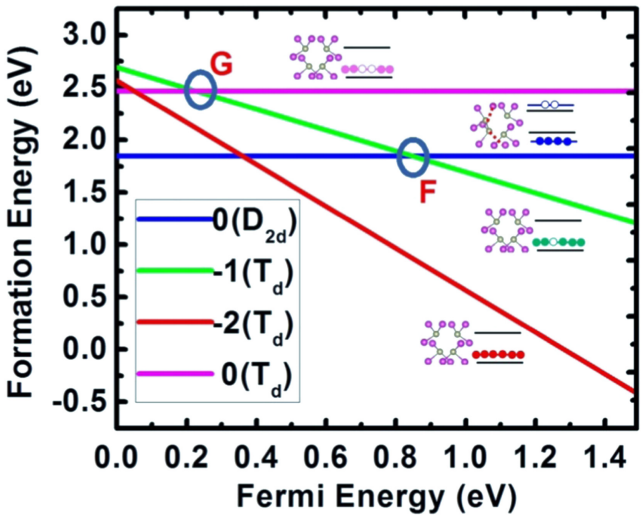

Figure 5. HSE06 calculated formation energies of Cd vacancy at different charge states and structural configurations as functions of Fermi energies (referenced to the VBM). The inset shows the atomic and electronic configurations for different states. The pink balls are Cd and the light yellow balls are Te.

Table 1. Calculated electron capture rate constants B_n and hole capture rate constants B_p through defect levels at points C, D, E, F, and G in figures 4 and 5.

level	B_n ($cm^3\ s^{-1}$)	B_p ($cm^3\ s^{-1}$)
C(Te_{Cd})	2.50×10^{-7}	—
D(Te_{Cd})	1.69×10^{-10}	1.67×10^{-7}
E(Te_{Cd})	—	2.46×10^{-6}
F(V_{Cd})	3.54×10^{-10}	1.55×10^{-11}
G(V_{Cd})	—	3.95×10^{-8}

recombined through only one level (such as point D) as has usually been assumed, it is also impossible for Te_{Cd}^{2+} to cause strong recombination in CdTe, because electron trapping through the point D defect level is also very slow with an electron capture rate constant of $1.69 \times 10^{-10}\ cm^3\ s^{-1}$.

However, we identified a two-level recombination mechanism, i.e. electron trapping happens through a defect level at point C, while hole trapping through a defect level at point E, which can drastically enhance the recombination process. We note that the energy barrier from the T_d 1+ state to the C_{3v} 1+ state is actually (close to) zero, which means the time needed for the structural transition is very short compared to the time to trap one hole. Then, we can expect that the defect, which needs a relatively longer time to trap one hole, will soon change to another configuration after trapping one electron and before hole trapping. This is also why we did not consider the hole trapping at point C in table 1. One might wonder whether trapping one electron through the point C defect level then relaxing to the C_{3v} Te_{Cd}^{+} state is the same process as directly trapping one electron through the defect level at point D. The easy relaxation from the T_d Te_{Cd}^{+} state to C_{3v} Te_{Cd}^{+} state after accepting one electron can be considered as strong electron–phonon coupling, which can enhance the electron-trapping rate through the defect level at point D. Nevertheless, our direct calculation indicates that, under harmonic approximation of the phonon mode, the direct electron trapping through the point D defect level is slow. This could be a breakdown of the phonon harmonic approximation (for trapping through point D), which has been used in the formalism, while the trapping through point C can be described by the harmonic approximation. But it could also be that the electronic configuration of the C_{3v} Te_{Cd}^{+} state can be considered as a different electronic configuration compared to the case of the T_d Te_{Cd}^{+} state and then the transition at defect levels C and D are clearly distinct. In either case, it means a fast harmonic oscillator like (e.g. as described by the multi-phonon quantum formula, or the classical Marcus theory) direct transition through the defect level at point D is impossible. For the transition at point C, after the defect traps one electron and becomes Te_{Cd}^{+}, the phonon degree of freedom should quickly relax to the T_d ground state since it has the same symmetry as before the transition and it has a relatively much smaller displacement. In other words, the T_d Te_{Cd}^{+} state is a local basin in the high-dimensional energy manifold of the phonon degree of freedom after the charge transition, which only has one degree of freedom leading to the C_{3v} Te_{Cd}^{+} state. After that, it could relax to the C_{3v} Te_{Cd}^{+} state. Thus, it will be more descriptive and meaningful to describe the process as first trapping one electron through the defect level at point C with T_d symmetry, then quickly relaxing to the ground state with C_{3v} symmetry. The same can be said for trapping a hole through the defect level at point E with C_{3v} symmetry, then relaxing to the ground state of Te_{Cd}^{2+} with T_d symmetry (figure 4). The hole trapping through the point E defect level is easy, because the Te_{Cd}^{2+} state has the same C_{3v} symmetry as the Te_{Cd}^{+} state. The difference is that the energy barrier from the Te_{Cd}^{2+} state with C_{3v} symmetry (blue line in figure 4) to the Te_{Cd}^{2+} state with T_d symmetry (red line in figure 4) is now 0.23 eV according to our NEB calculations based on the HSE06 functional. Using the transition state theory [76], we can estimate the time it takes for the 2+ state to transform from the C_{3v} structure to the T_d structure, which is given by $1\Big/\left[\nu \exp\left(-\frac{E_a}{k_B T}\right)\right]$, where E_a is the energy barrier and ν is the transition rate. Using $E_a = 0.23$ eV and the calculated $\nu = 1.02$ THz, the time needed to complete the transition at $T = 300$ K is about 6.81 ns. Compared to the time costs for the electron and hole trapping, which are 186 and 18.9 ns, respectively, estimated from $\tau = (B_{n,p}N_D)^{-1}$, the structural transition is very quick. This is reasonable and consistent with the fact that the dominant state of Te_{Cd}^{2+} has T_d symmetry in p-type CdTe; otherwise there could be accumulations of the Te_{Cd}^{2+} state with C_{3v} symmetry during the recombination process if the barrier is very large.

Thus, we describe the whole recombination process mediated by Te_{Cd}^{2+} through two levels in p-type CdTe as follows. First, the electron trapping, which is also the key step, happens through the defect level at point C with a large capture rate constant and changes the T_d Te_{Cd}^{2+} state to the T_d Te_{Cd}^{+} state. Second, the T_d Te_{Cd}^{+} state changes to the C_{3v} Te_{Cd}^{+}

state with nearly zero barriers due to structural relaxation or phonon vibration. Third, the hole trapping happens through the defect level at point E with a large capture rate constant and changes the C_{3v} Te_{Cd}^{+} state to the C_{3v} Te_{Cd}^{2+} state. Fourth, the C_{3v} Te_{Cd}^{2+} state changes to the T_d Te_{Cd}^{2+} state by overcoming an energy barrier of 0.23 eV with the help of phonon vibrations, finishing the whole recombination loop. The whole process is determined mainly by the slowest step. According to our calculation, the slowest step in the Te_{Cd}^{2+} recombination process is the first step, which has an estimated carrier lifetime of 186 ns. We note that our result is in good agreement with a recent experimental measurement of *p*-type CdTe grown by the molecular beam epitaxy method with only intrinsic defects [81], which has a hole density of 3×10^{14} cm^{-3} and a bulk SRH lifetime of 360 ns.

To summarize our results for the intrinsic defect properties of CdTe, we find that if intrinsic CdTe is grown under Te-rich condition, CdTe can only be slightly *p*-type doped with low hole density, due to the relatively deep acceptor level of Cd vacancy. Most importantly, the Te-rich condition can lead to the formation of a large amount of Te_{Cd}^{2+}, which is the dominant non-radiative recombination center and will limit the carrier lifetime. Therefore, it is worth considering another option, where CdTe is grown under Cd-rich condition and achieves *p*-type doping using extrinsic dopants, as discussed below.

4. Doping CdTe *p*-type using extrinsic elements

As shown in our previous section, to improve the V_{oc} and hole density of *p*-type CdTe solar cells, we have to consider extrinsic doping to overcome the intrinsic limit caused by deep V_{Cd} levels. Two options are, using group V elements such as P and As to replace Te under Cd-rich condition and using group I elements such as Na to replace Cd under Te-rich condition.

4.1. Group V elements

Group V element doping in CdTe has been studied for more than half a century. Experimental results show that high hole density exceeding 10^{16} cm^{-3} indeed can be obtained with P or As doping [82–89]. However, several problems still remain unclear. First, hole densities are reported to be pinned to $10^{16} \sim 10^{18}$cm^{-3} and adding more P and As does not seem to help the enhancement of hole densities [87]. Second, the stability of P and As doping is rarely discussed and the high-efficiency CdTe solar cell based on P and As doping is rarely reported. Due to the lack of a deep understanding and quantitative study of P and As doping in CdTe, no breakthrough has been made so far to obtain high-performance CdTe solar cells using P and As doping.

P and As are expected to replace Te in CdTe and act as acceptors, because P and As have one fewer electron than Te. Our calculations confirm that for neutral defects, the most stable ones are P and As substitutions on Te sites, P_{Te} and As_{Te}, respectively, whereas other defects such as P and As interstitials all have higher formation energies (figure 6), especially under Cd-rich condition. At the neutral states with T_d symmetry, P_{Te} and As_{Te} have seven electrons. Two electrons will fill the single (without count of spin) *s*-like a_1 state deep in the valance band, and the other five electrons will occupy the three-fold-degenerate *p*-like t_2 state with one hole left. Because this t_2 level is just above the VBM of CdTe, it will be easy for P_{Te} and As_{Te} to accept one additional electron from the VBM and create holes in the valance band of CdTe. Our calculated acceptor transition energy levels of P_{Te} and As_{Te} are 0.07 and 0.10 eV, respectively, above the VBM of CdTe (figure 6). These values are in agreement with previous calculations [33] and experimental results [82, 88, 90] and shallower than the acceptor level created by Cu, showing the advantage of anion substitution for making *p*-type CdTe. However, as for some acceptor defects in tetrahedral semiconductors, P and As may form AX centers, converting them from acceptors to donors [91, 92]. When an AX center is formed, a P (or As) atom will move toward its neighboring Te atom and form a P–Te (or As–Te) bond by breaking their two bonds with Cd, as shown in figure 6(c). In this case, the three-fold-degenerated defect states under T_d symmetry will split into a doubly degenerate *e* state and a single *a* state. If the *e* state is fully occupied and the *a* state is fully empty, it will gain a significant amount of electronic energy. The AX center is stabilized when the electronic energy gain is larger than the energy cost in breaking two anion–cation bonds [66]. Different from the LDA results in [33], our HSE06 calculations show that both P_{Te} and As_{Te} can form AX centers when they are at the +1 charged states with the stability energies [defined as $\Delta E\,(AX) = E\,(AX, +1) - E\,(P_{Te}, +1)$] of 0.50 and 0.52 eV, respectively. This difference could be because HSE06 tends to localize the defect wavefunction, which leads to a large splitting of the *a* and *e* states (figure 6(c)), thus making AX centers more stable. Taking into account the above discussions, we show our calculated P and As defect formation energies in CdTe under Te-rich and Cd-rich growth conditions in figures 6(a) and (b), respectively, where the following chemical potential conditions are used: $\mu_{Cd} + \mu_{Te} = -1.17$ eV, $3\mu_{Cd} + 2\mu_{P} < -0.57$ eV, and $3\mu_{Cd} + 2\mu_{As} < -0.46$ eV. As can be seen in figure 6, due to the self-compensation of P_{Te}^{-} by its AX center P_{Te}^{+}, the Fermi level will be pinned around the J point at 0.32 eV above the VBM in figure 6(a) under equilibrium growth conditions, at which P_{Te}^{-} and P_{Te}^{+} have the same formation energy. A similar case occurs with As doping, where the Fermi level will be pinned around the K point at 0.36 eV in figure 6(a) under equilibrium growth conditions.

Our thermodynamic simulation confirmed the Fermi level pinning. As can be seen in figure 7, no matter at what temperature phosphorus-doped CdTe is grown, the Fermi level cannot be lower than 0.32 eV under equilibrium growth conditions. However, we note that a high hole density close to $10^{17} \sim 10^{18}$ cm^{-3} can be achieved when P-doped CdTe is grown at $T = 800$ and 1200 K. This is because strong band-edge thermal excitations at a high temperature will help to keep the Fermi level above point J, thus making more phosphrous prefer to form the acceptor P_{Te}^{-} than the donor P_{Te}^{+}. That is to say, there is a larger density difference between $n\,(P_{Te}^{-})$ and $n\,(P_{Te}^{+})$, resulting in a high hole density. Generally

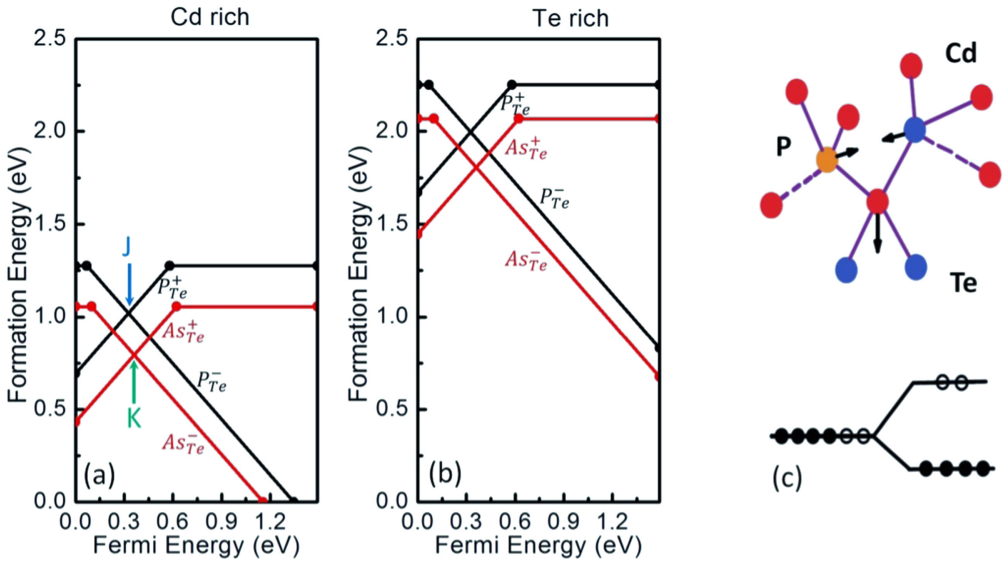

Figure 6. Formation energies of P_{Te} and As_{Te} as functions of Fermi levels under (a) Cd-rich condition and (b) Te-rich condition. At point J or K, the negatively charged substitutional defect with T_d symmetry has the same formation energy as the positively charged AX center. Note that neutral defects are not stable against decomposition to their charged states. (c) Schematic diagram to show how AX centers are stabilized by lattice distortions.

speaking, the higher the growth temperature, the more likely P is to form acceptors rather than donors before P_{Te}^{-} and P_{Te}^{+} compensate strongly with each other.

To overcome the Fermi level pinning caused by self-compensation, we adopt the rapid-cooling methods as discussed in section 2. Because of the linear relation of Fermi energy on k_BT, equation (7) shows that the Fermi level can be lowered toward the VBM if we can maintain high hole density when the temperature is reduced. Because the substitutional acceptor has a shallow acceptor level, which can be easily ionized even at room temperature, the hole density is mainly determined by the density difference of $n(P_{Te}^{-})$ and $n(P_{Te}^{+})$. A high $n(P_{Te}^{-}) - n(P_{Te}^{+})$ density difference can be achieved if we grow the sample at high temperature. When we lower the temperature quickly to a low temperature (such as $T = 300$ K) to sustain the high $n(P_{Te}^{-}) - n(P_{Te}^{+})$ density difference, the Fermi level can be pushed down beyond the pinning point J. The right panels of figure 7 show our simulated results. As can be seen, the Fermi level after rapid cooling from $T = 800$ K is lowered toward the acceptor transition energy level, whereas the hole density as high as 10^{17} cm^{-3} can still be achieved when 10^{18} cm^{-3} P is incorporated into CdTe. Non-equilibrium cooling from $T = 1200$ K to $T = 300$ K gives similar results. However, we also note that when the total concentration of P exceeds 10^{18} cm^{-3}, the resulting Fermi level increases slightly and the hole density decreases. This is because at a very high P concentration, more P_{Te}^{+} is formed, and its amount does not change after non-equilibrium cooling. On the other hand, large amounts of P_{Te}^{-} will convert to neutral P_{Te}^{0} after non-equilibrium cooling. Therefore, the hole density p_0 will decrease, leading to the increase in Fermi level at very high P density. Our simulations, therefore, indicate that the optimal amount of P incorporated into CdTe is about 10^{18} cm^{-3}. Similar results are obtained in the As doping case.

Our quantitative studies can well explain the observed hole density pinning problem [87] and provide helpful information about P and As doping in CdTe. One thing we have to point out is that the long-term stability of P and As as p-type dopants could be challenging, because based on our calculation, the diffusion barrier of P_{Te}^{+} from the T_d symmetry site to the AX site is less than 1 eV. Applying strain and alloying CdTe with ZnTe, are expected to improve the stability against the formation of the AX centers, because ZnTe has a smaller lattice constant and the Zn–Te bond is stronger than the Cd–Te bond, so P_{Te} is expected to have lower formation energy, whereas the AX center is expected to have higher formation energy in ZnTe.

4.2. Group I alkaline elements

Group I elements such as Li, Na, and K are also considered as potential good acceptors in CdTe [33, 93–95]. Here we re-examine Na-related defects using HSE06 functionals. We calculated the formation energies of Na-related defects in CdTe as functions of Fermi levels, as shown in figure 8. The $(0/-)$ level of Na_{Cd} is about 0.05 eV above the VBM and the $(0/+)$ level of Na_i is 0.04 eV below the CBM of CdTe, in good agreement with previous calculations [33]. Similar to group V doping, Na doping is also self-compensated under equilibrium growth conditions and the Fermi level will be pinned relatively deep above the VBM. For example, under Te-rich condition, the Fermi level will be always higher than point N, which is about 0. 36 eV, as also confirmed by our thermodynamic simulations in figure 9. Similarly, this self-compensation can be overcome by the rapid-cooling method. As shown in the right panel in figure 9, after rapid cooling, a Fermi level of about 0.1 eV can be achieved with hole density above $\sim 10^{17}$ cm^{-3} when about 10^{18} cm^{-3} Na is incorporated.

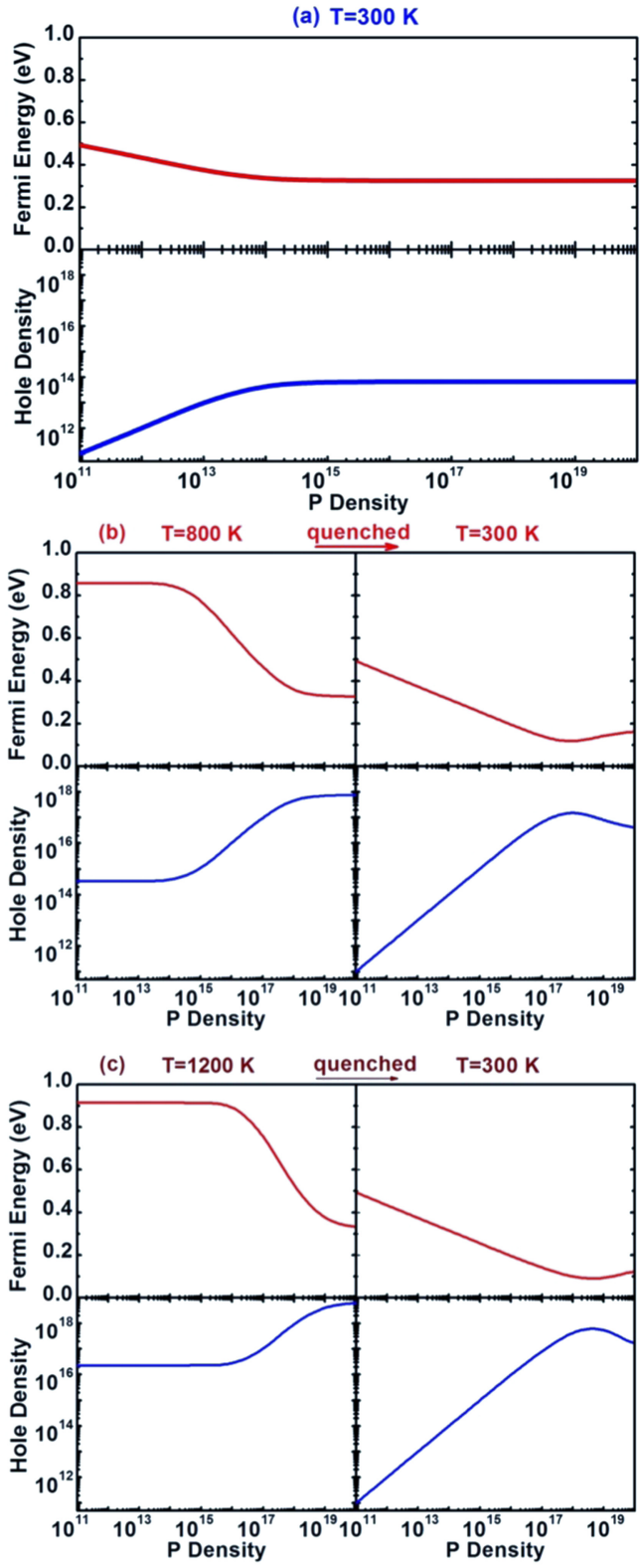

Figure 7. Fermi level and hole density as functions of P density under thermodynamic equilibrium growth condition are shown in (a) at $T = 300$ K and the left panels of (b) at $T = 800$ K and (c) at $T = 1200$ K, respectively. The right panels of (b) and (c) show the Fermi level and hole density as functions of P density after non-equilibrium cooling to $T = 300$ K. The densities are given by number per cm^3.

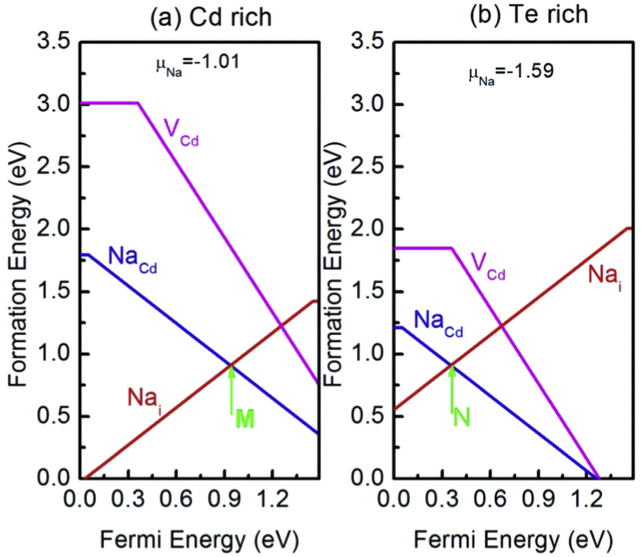

Figure 8. Formation energies of Na_{Cu} and Na_i as functions of E_F under (a) Cd-rich condition and (b) Te-rich condition.

Our results agree well with the experiments [94]. A recent experimental work also reported that a V_{oc} value as high as 929 meV was achieved in Na-doped single-crystal CdTe solar cells [93]. In this work, Na is also found to cause instability of performance. This is possible since Na_{Cd} is unstable at low Fermi energy against Na_i and other Na-related defects such as donor–acceptor complex. Our recent studies show that in $Cu_{Cd} + Cd_i$ defect complex, Cu can easily be kicked back to the interstitial site and then Cu interstitial can diffuse away and compensate Cu_{Cd} doping. Similar effects may also occur in the case of Na doping in CdTe. More work on Na-related defect complex is needed in the future.

To summarize our results for the extrinsic doping of CdTe using group VA and group IA alkaline elements, we have found that both group VA and group IA alkaline elements, in principle, can achieve good p-type doping in CdTe single crystals. While group VA elements might have a stability issue due to the conversion of the acceptor state to the AX donor state, group IA alkaline elements might suffer a knock-on effect of neighboring interstitial atoms. We are aware that a recent experimental work reported a high V_{oc} value of 1.05 V that has been realized in phosphorus-doped CdTe [96].

5. Cu and Cl treatment in CdTe

Experimentally, it is well known that both Cu and Cl treatments are crucial for CdTe solar cells to obtain high energy conversion efficiency. However, the exact roles that Cu and Cl play in enhancing CdTe solar cell efficiency are still under debate and many explanations and mechanisms have been proposed. For example, for Cl, suggested mechanisms include improving grain growth and recrystallization [27, 97],

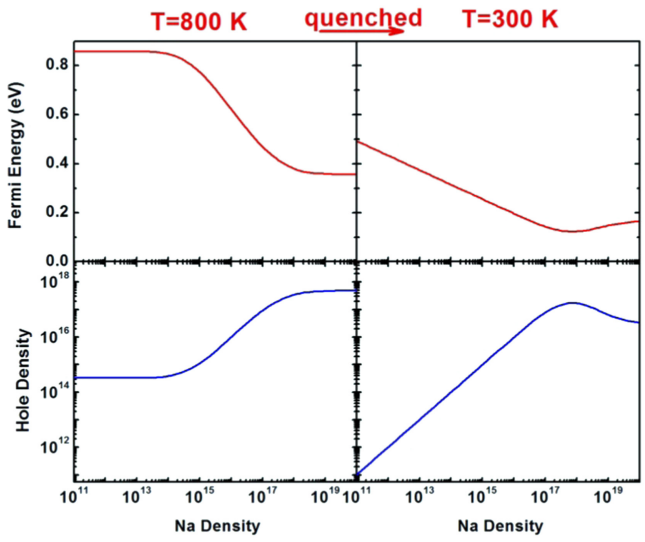

Figure 9. Fermi level and hole density as functions of Na density at $T = 800$ K under thermodynamic equilibrium growth condition are shown in the left panel, and the right panel shows the Fermi level and hole density as functions of Na density after rapid cooling to $T = 300$ K. The densities are given by number per cm^3.

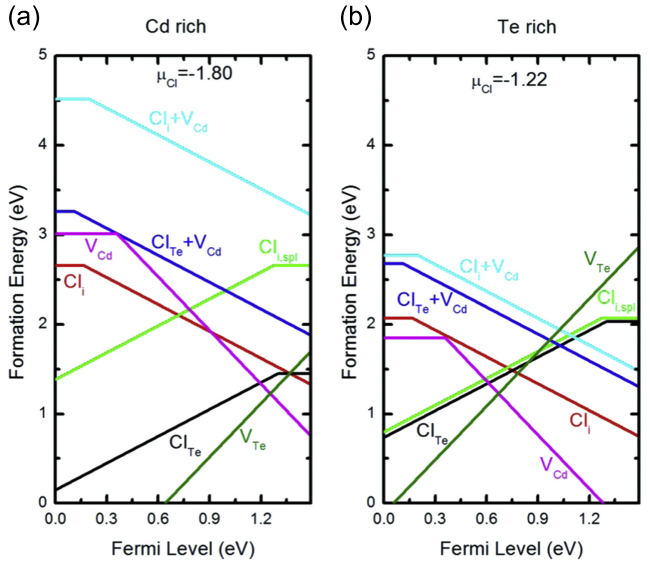

Figure 10. Cl-related defect formation energies in CdTe as functions of Fermi levels under (a) Cd-rich condition and (b) Te-rich condition. The chemical potential conditions are $\mu_{Cd} + \mu_{Te} = -1.17$ eV and $\mu_{Cd} + 2\mu_{Cl} < -3.60$ eV.

enhancing S diffusion from CdS to CdTe [98, 99], passivating deep defect levels within the band gap [37, 97, 100], and helping carrier collection [101–104]. Although Cl incorporation indeed helps to improve CdTe solar cell efficiency, some works on single-crystal CdTe indicate, on the other hand, that too much Cl will induce hole traps deep in the middle of the CdTe band gap, thus limiting the solar cell performance [46, 101]. The fact that Cl treatment is only necessary in polycrystalline CdTe, but not in single crystals suggests Cl may have a strong impact on passivating CdTe GBs. For Cu, the common idea that the function of Cu is to reduce the back contact barrier still dominates in this field [105, 106], while some recent works support the fact that Cu plays an important role in enhancing *p*-type doping in CdTe [107, 108]. Here, we use first-principles calculations to study both Cl- and Cu-related defects in bulk CdTe and their segregations at CdTe grain boundaries.

5.1. Cu- and Cl-related defects in bulk CdTe

First, let us discuss Cl doping in bulk CdTe. We find that Cl can either replace Te and form Cl_{Te} or go to interstitial sites. Because Cl has one more electron than Te, Cl_{Te} is expected to be a donor, with a calculated $(0/+)$ transition energy level of 0.19 eV below the CBM, as can be seen in figure 10. Cl interstitial defects are complicated. For the neutral interstitial, Cl is found most stable at the B_c site in reference [51] due to level splitting caused by reduced symmetry. For -1 charged interstitial, Cl is stabilized at the center of the tetrahedron surrounded by four Cd, as expected. In this case, Cl interstitial behaves as a shallow acceptor with a $(0/-)$ transition energy level of 0.17 eV above the VBM. However, when Cl interstitial is positively charged, Cl interstitial can lower its energy by forming a Cl–Te bond at the Te atomic site, as shown in figures 11(a) and (b), which is similar to the behavior of neutral Te interstitial in [51]. In this case, Cl interstitial will act as a donor with a $(0/+)$ level of 0.22 eV below the CBM. Beside the point defects, Cl can also form defect complexes such as the A center ($Cl_{Te} + V_{Cd}$). When the A center forms, the additional electron of Cl_{Te} will spontaneously fill the empty defect state of the Cd vacancy. Initially, the neutral Cd vacancy has two holes, which lead to a large structural distortion and level splitting, resulting in a relatively deep negative U $(0/2-)$ acceptor level at 0.36 eV, as shown in figure 2. When Cl_{Te} is present near the Cd vacancy, charge transfer from Cl_{Te} to V_{Cd} will happen, making the structural distortion of the Cd vacancy not favored anymore, as shown in figure 11(c). As a result, the A center has a shallow $(0/-)$ acceptor level of about 0.11 eV above the VBM, in agreement with the experimental result [30]. In this sense, A center indeed can improve the *p*-type doping in CdTe. However, the concentration of A center will be limited by the amount of Cd vacancies. Once the Cd vacancies are all consumed, A center will have higher formation energy than Cl interstitial and Cl_{Te}. The consequence is that negatively charged Cl interstitial will compensate the positively charged Cl interstitial and Cl_{Te}, pinning the Fermi level in the middle of the band gap and leading to deep levels in Cl-doped CdTe. Our calculated results can be compared to the experimental results in [46, 101], which suggest that too much Cl incorporation into CdTe could be harmful.

For Cu doping in CdTe, it can form two important defects. One is the substitutional defect Cu_{Cd} and the other is Cu interstitial. Because Cu has one valance electron less than Cd, Cu_{Cd} behaves as an acceptor. Due to the anion *p*—Cu *d* coupling effect in tetragonal semiconductors, Cu substitutions usually have deep acceptor levels [109]. However, in CdTe,

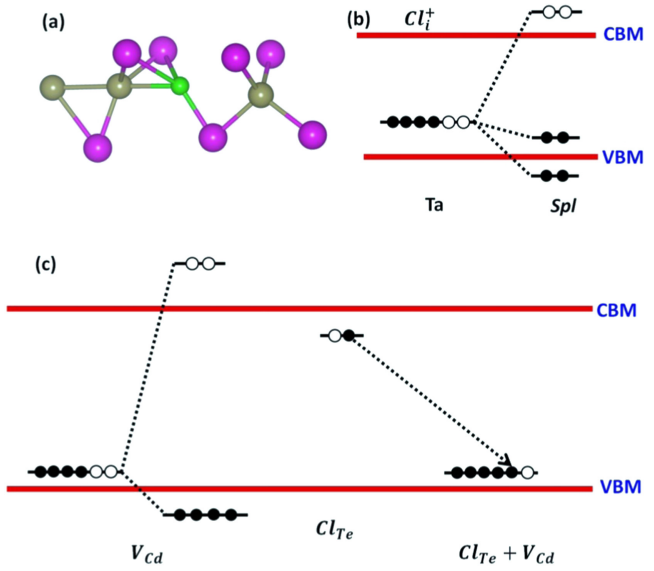

Figure 11. (a) The most stable structure of Cl_i^+, where Cl forms a bond with Te. This kind of structure is referred to as a split interstitial (*Spl*) structure and the pink balls are Cd atoms, the brown balls are Te atoms and the green balls are Cl atoms. (b) The diagram shows how the *Spl* structure is stabilized by level splitting. (c) The diagram shows how the neutral Cd vacancy is stabilized by level splitting and how the A center makes a shallow acceptor level in CdTe.

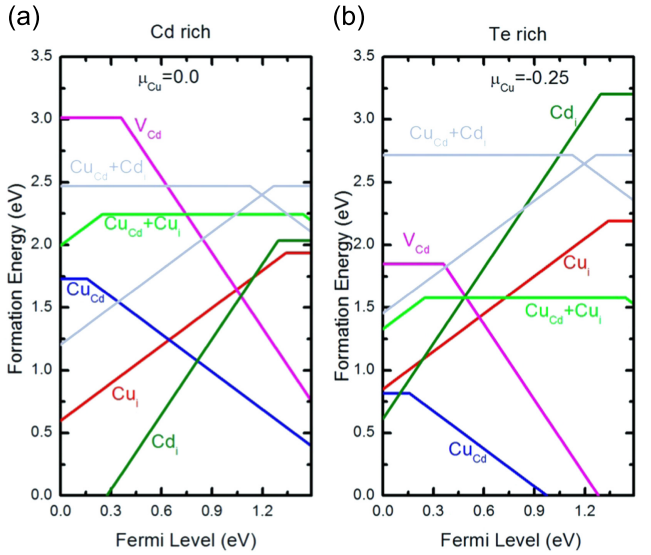

Figure 12. Cu-related defect formation energies in CdTe as functions of Fermi levels under (a) Cd-rich condition and (b) Te-rich condition. The chemical potential conditions are $\mu_{Cd} + \mu_{Te} = -1.17$ eV and $\mu_{Cu} + \mu_{Te} < -0.25$ eV.

p–d coupling is suppressed because of the large lattice constant. As a result, Cu_{Cd} in CdTe has a relatively shallow $(0/-)$ acceptor level of 0.16 eV above the VBM, as shown in figure 12. Our HSE06 result differs slightly from previous LDA calculation [33] because a supercell size correction of about 0.06 eV is used in the current calculation. Experimentally, this level varies between 0.15 and 0.35 eV [110–115]. However, compared to the calculated acceptor level of Cd vacancy, which is 0.36 eV above the VBM, the Cu_{Cd} $(0/-)$ level is still shallower. As a result, Cu doping in CdTe should be able to improve the *p*-type conductivity in CdTe, as observed experimentally [107, 108]. Furthermore, under Te-rich condition, the Cu substitutional defect always has lower formation energy than Cu interstitial (see figure 12). Thus, the dopant self-compensation can be suppressed by properly controlling the growth conditions. Although the Cu_{Cd} level is still relatively deep compared to acceptor levels in other solar cell materials such as $CuInSe_2$ and Cu_2ZnSnS_4, Cu is the best cation-substituting acceptor up to now. More importantly, besides *p*-type doping, Cu also plays an important role in forming the low-resistance back contacts, although Cu also induces stability problems due to its fast diffusion in bulk CdTe [51, 53, 116–119], which will also be discussed later.

5.2. Cu and Cl segregation at CdTe GBs

Now that we have clarified the Cl- and Cu-related defects in bulk CdTe, we turn to discuss their behaviors in GBs. We want to point out that the defect behaviors at GBs might vary with different GB structures. Here, we focus our study on the two typical and most energetically favorable GBs, $\Sigma3(111)$ and $\Sigma3(112)$ GBs [55, 120–122], as shown in figure 13. The $\Sigma3(111)$ GB can be seen as a stacking fault between the zinc-blende and wurtzite structures. Because there are no dangling bonds or wrong bonds in $\Sigma3(111)$ GB, its formation energy is very low and this GB is expected to have large populations in polycrystalline CdTe [55]. The Te-core $\Sigma3(112)$ GB, on the other hand, contains Te–Te wrong bonds, which will form a deep gap state and be harmful for CdTe electronic properties. Because this GB also has relatively low formation energy compared to other GBs, Te-core $\Sigma3(112)$ GB is also expected to exist in significant amounts in CdTe.

First, we studied the segregation of Cu and Cl in their neutral and charged defect states. Figures 14 and 15 show our calculated results in these two GBs. As can be seen, in general, Cu and Cl show little segregation at $\Sigma3(111)$ GB as expected from the similarity between this GB and bulk, except that Cl interstitial has segregation energy of about 0.2 eV. This is because the stacking fault at $\Sigma3(111)$ GB gives Cl interstitial more space to stay, as shown in figure 16(a). On the other hand, the energy of neutral Cu interstitial does not sensitively depend on the space, but the *s-d* coupling [51, 116]. As a result, Cu interstitial does not show segregation. Things are different at Te-core $\Sigma3(112)$ GB. For Cl interstitial, it behaves similarly to at $\Sigma3(111)$ GB. Here, the Te-core $\Sigma3(112)$ GB offers Cl interstitial even larger space as shown in figure 16(b) and as a result, the segregation energy of Cl interstitial is as large as 1.2 eV for both neutral and charged states. For Cl substitution, because in this case Te–Te wrong bond is broken due to the smaller size of Cl (figure 16(c)), each Te dangling bond state will relax back into the valence band. As each Te dangling bond has 1.5 electrons (see [37]), Cl will transfer 0.5 electrons to each Te and passivate the dangling bond. Consequently, there exists a

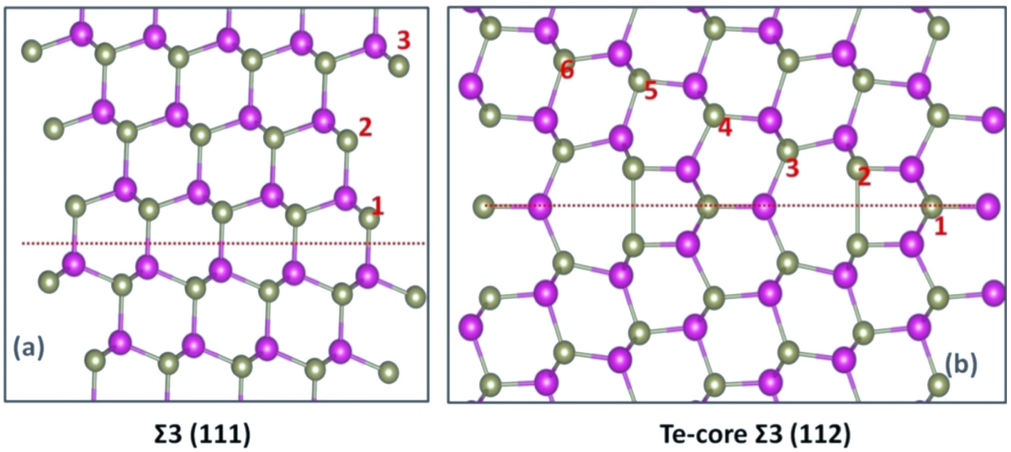

Figure 13. Two CdTe GBs used in this work. (a) $\Sigma3(111)$ GB without wrong bonds and (b) Te-core $\Sigma3(112)$ GB with the Te–Te wrong bonds. The pink balls are Cd atoms and the brown balls are Te atoms.

large energy gain, resulting in the strong segregation of Cl_{Te}. When Cl_{Te} is $+1$ charged, charge transfer still happens from the VBM of CdTe to the Te dangling bond, resulting in a smaller but still large energy gain. Consequently, Cl_{Te}^{+} also shows relatively strong segregation. Our results are consistent with experimental observations [101–104] and previous studies [37].

Similarly, for neutral Cu interstitial at Te-core $\Sigma3(112)$ GB, Cu sits near the middle of the Te–Te bond (see figure 16(e)), thus breaking the Te–Te state. The one extra electron of Cu interstitial transfers to the two Te dangling bonds, resulting in a large energy gain and strong segregation of neutral Cu interstitials at Te-core $\Sigma3(112)$ GB. When Cu interstitial becomes positively charged, charge transfer from the VBM of CdTe to the Te dangling bonds still causes the segregation of Cu interstitial. For Cu substitutions at Te-core $\Sigma3(112)$ GB (figure 16(f)), the segregation of neutral defect can be explained as follows. Because Cu_{Cd} can introduce a partially occupied acceptor state near above the VBM, the fully occupied Te–Te state can thus transfer one electron to the acceptor state with an energy gain. However, when Cu_{Cd} is negatively charged, the acceptor state is now fully occupied and there is no charge transfer from the Te–Te state anymore. As a result, after Cu_{Cd} is negatively charged, the segregation of Cu_{Cd} is strongly suppressed. We note that Cu segregation is reported experimentally [12, 108, 119] which can be attributed to Cu interstitials or neutral Cu on Cd sites at Te-core $\Sigma3(112)$ GBs.

Through the above studies, we can conclude for this section that the main role of Cl should lie with its interactions with GBs, while Cu can both improve *p*-type doping in the bulk region and interact with GBs. However, to fully understand the roles of Cu and Cl, we need to take into account other factors, such as the interactions between defects, the formation of defect complexes, and the non-radiative recombination that could be caused by Cu- and Cl-related defects. These aspects are worth studying in the future.

6. Impurity diffusion in CdTe

Impurity dopants are often introduced into semiconductor systems through diffusion. In CdTe, dopants can include Na, Cu, Cl, P, As, etc. Besides, impurity can be related to the stability of device performance by changing its locations and doping behaviors through diffusion. For example, Cu can induce performance instability of CdTe solar cells, because Cu is a fast diffuser. As a result, knowledge of impurity diffusion in CdTe is of great importance for effectively controlling dopants and improving the device stability.

Usually, for a substitutional defect, its diffusion should be with the aid of vacancies. During diffusion, a substitutional atom jumps from a regular site into a neighboring vacancy site in executing the unit step. In addition to the probability of crossing the activation barrier along the path, the probability of the neighboring site being vacant also has to be considered. Hence, substitutional diffusion is generally 4–6 orders of magnitude slower than its interstitial diffusion. As a result, here we mainly discuss interstitial diffusion in CdTe and focus on group IA (Li, Na, K), Cu, Cl, and P.

6.1. Cation diffusion

First, we will see the diffusion of cation interstitials. For group IA elements (Li, Na, K), as expected, the most stable interstitial site is at the tetrahedral site due to the large spaces, and the barrier site is at or near the center of the two tetrahedral sites (denoted as *M* site). The neutral and $+1$ charged impurities have similar diffusion path and energy barriers due to the delocalized character of the impurities. There are two tetrahedral sites: T_c (next to cation) and T_a (next to anion). A larger atom like K prefers the T_c site, because of the large space and the smaller atom like Li prefers the T_a site due to larger Coulomb attraction. Na behaves in between, and it has minimum at the T_c site as for K, but with a smaller energy barrier (figure 17).

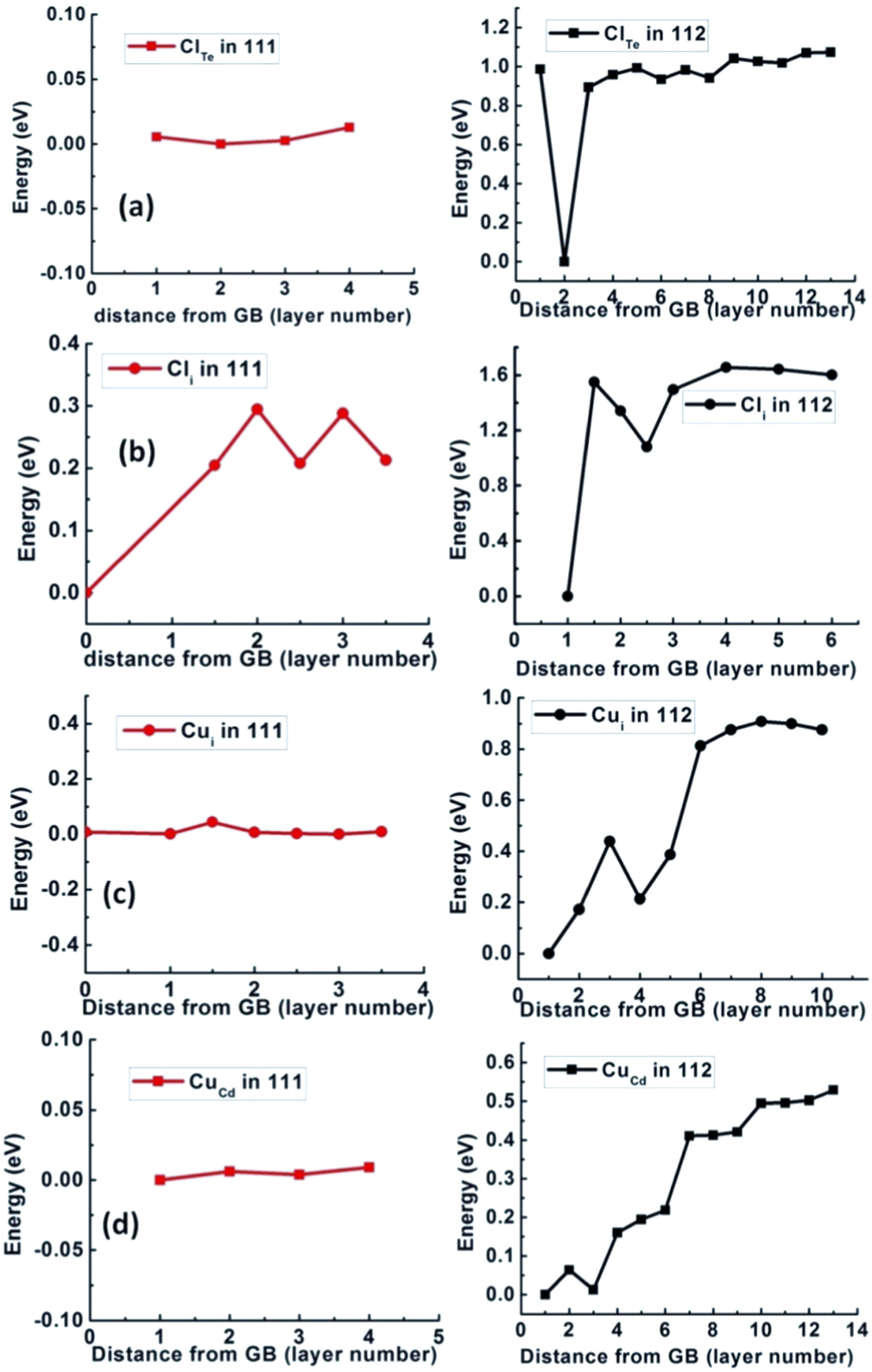

Figure 14. Segregation of charge-neutral Cu and Cl defects at GBs. (a) Cl_{Te}, (b) Cl_i, (c) Cu_i, and (d) Cu_{Cd} segregation at $\Sigma3(111)$ and Te-core $\Sigma3(112)$ GBs, respectively. The lowest energy points are set as zero, the layer numbers are labeled in figure 13, and the structural configurations are shown in figure 16.

The diffusion of Cu interstitial is different from the diffusion of group IA alkaline elements. Cu interstitial has its energy minimum at the *M* site, as shown in figure 18(b). This is because, due to the symmetry reduction at the *M* sites, the *s*-orbital-like conduction band is allowed to couple with Cu *d*-orbitals, which are fully occupied, highly delocalized and

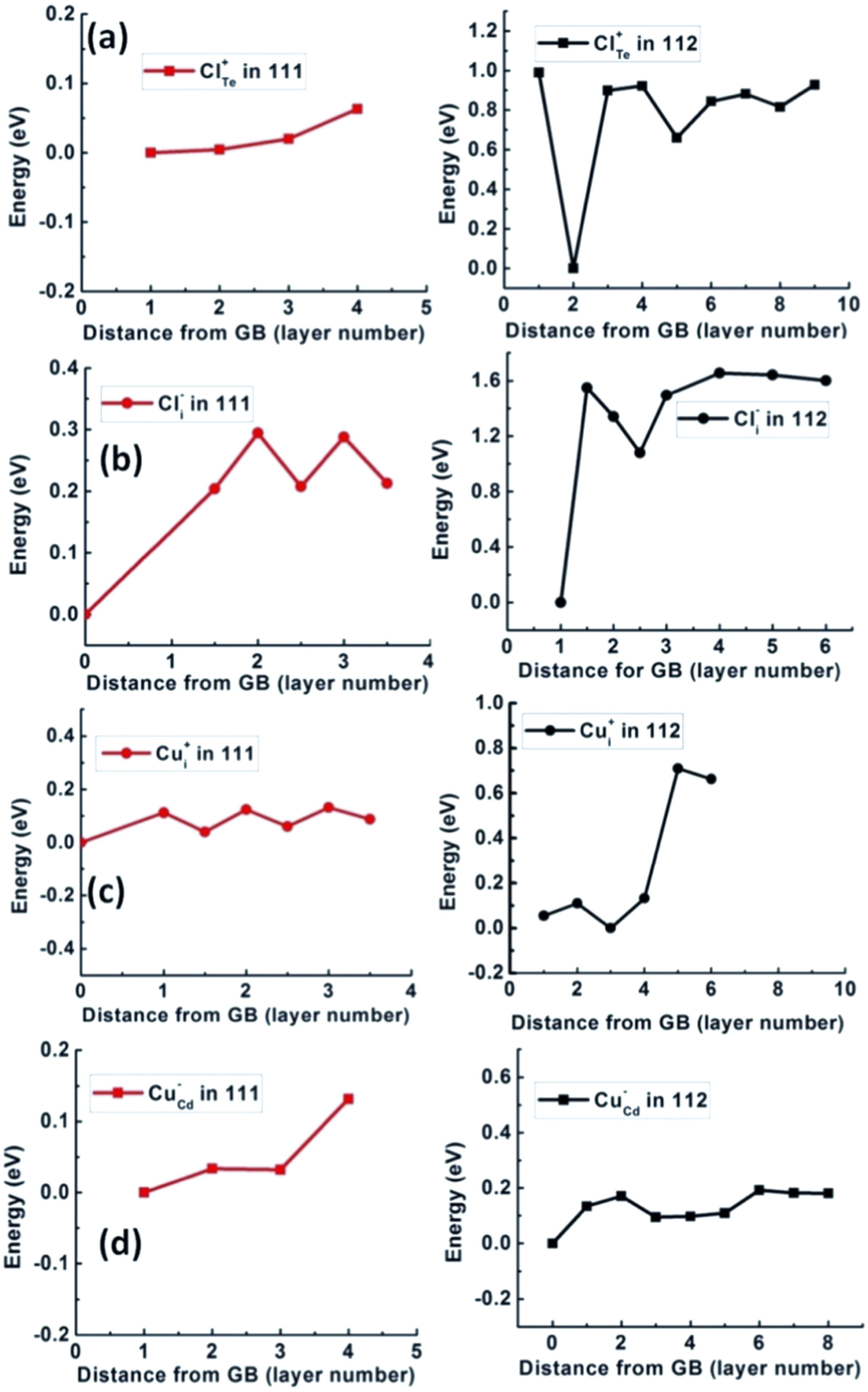

Figure 15. Segregation of charged Cu and Cl defects at GBs. (a) Cl^{+}_{Te}, (b) Cl^{-}_{i}, (c) Cu^{+}_{i}, and (d) Cu^{-}_{Cd} segregation at Σ3(111) and Te-core Σ3(112) GBs, respectively. The lowest energy points are set as zero, the layer numbers are labeled in figure 13, and the structural configurations are shown in figure 16.

shallow in energy. As a result, the *s–d* coupling at the *M* sites is strong enough to make Cu interstitials have large energy gain, leading to the energy minimum at the *M* sites. When Cu interstitials are positively charged, the energy gain at the *M* sites is even larger and thus Cu^{+}_{i} has larger energy barriers than neutral Cu_i. Due to the *s–d* coupling mechanism, Cu interstitials

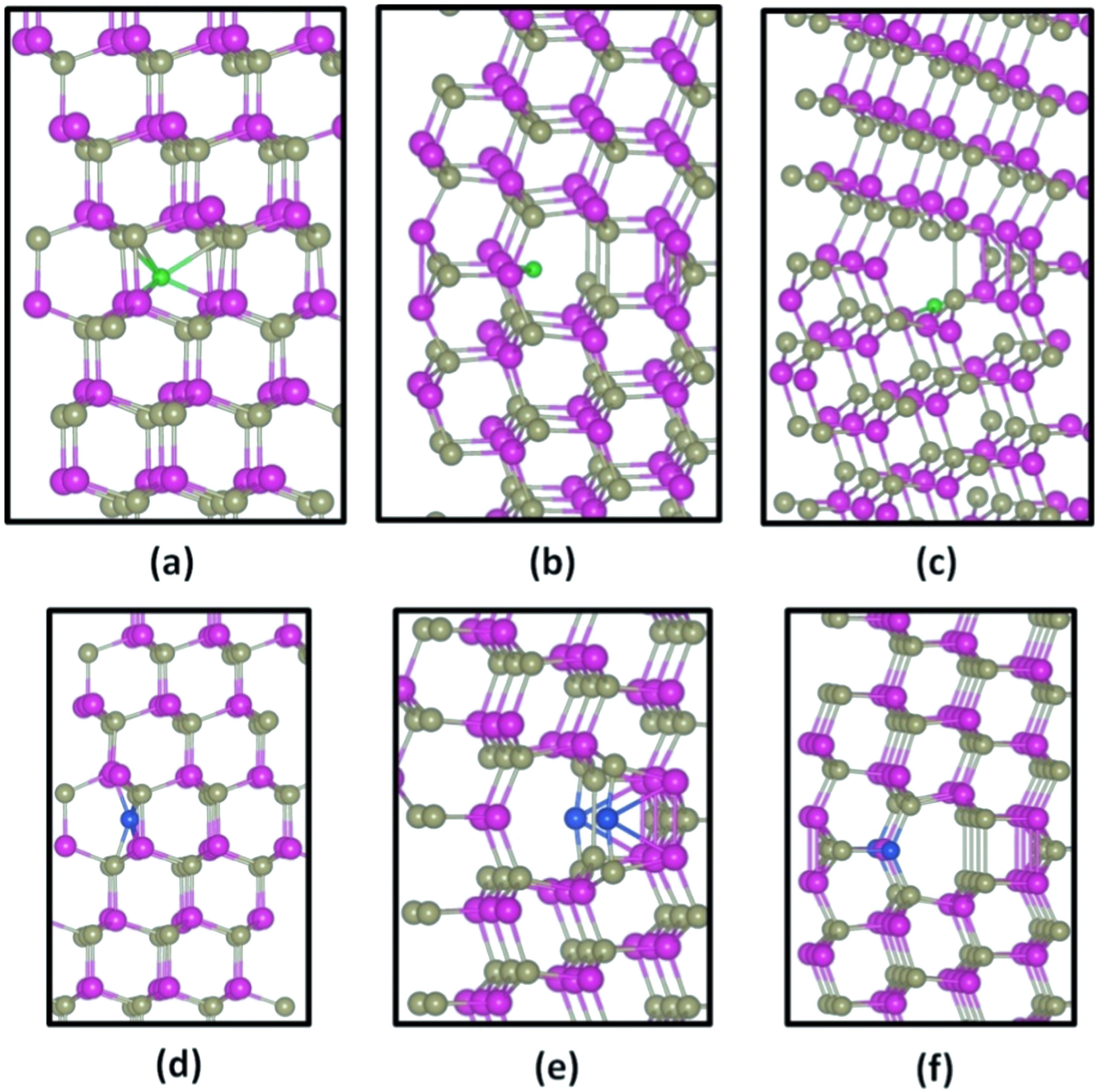

Figure 16. Structural configurations of Cu and Cl defects at CdTe GBs. (a) Cl interstitial at Σ3(111) GB. (b) Cl interstitial at Te-core Σ3(112) GB. (c) Cl substitution at Te-core Σ3(112) GB. (d) Cu interstitial at Σ3(111) GB. (e) Cu interstitial at Te-core Σ3(112) GB. (f) Cu substitution at Te-core Σ3(112) GB. The pink balls are Cd atoms, the brown balls are Te atoms, the green balls are Cl atoms, and the blue balls are Cu atoms.

generally have relatively low energy barriers, i.e. 0.28 eV for Cu_i and 0.46 eV for Cu_i^+. Consequently, Cu interstitials can diffuse relatively fast in CdTe, which contributes to the instability issues.

6.2. Anion diffusion

First, let us discuss the diffusion of Cl interstitial. Cl interstitial can have three charge states. Neutral Cl_i is most stable at the B_c site, which lies in the middle of two cations (see figure 19(b)). Due to the reduction of symmetry, the three-fold-degenerated states of Cl_i at the T_c site split into three separated states at the B_c site. When taking into account spin splitting, there can be large energy gain at the B_c site. Compared to PBE calculations, HSE06 strengthens the spin splitting considerably, i.e. 0.5 eV [51] by PBE compared to about 1.5 eV by HSE06 (see figure 19(c)). As a result, the energy gain at the B_c site can exceed the energy cost induced by strain, making the B_c sites local minimum. Consequently, the diffusion energy barriers for neutral Cl_i are calculated to

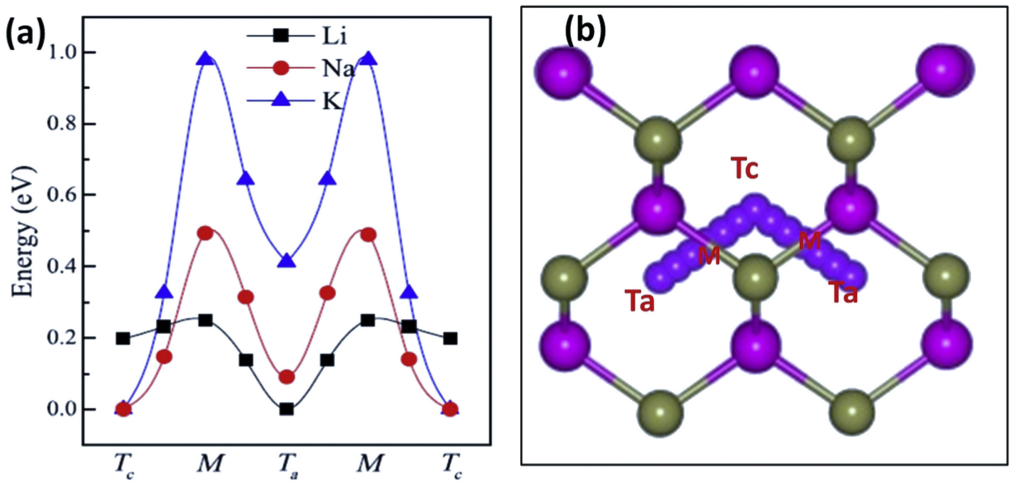

Figure 17. (a) Diffusion energies and (b) diffusion paths of group IA interstitials. The pink balls are Cd atoms, the brown balls are Te atoms, and the purple balls are group IA atoms.

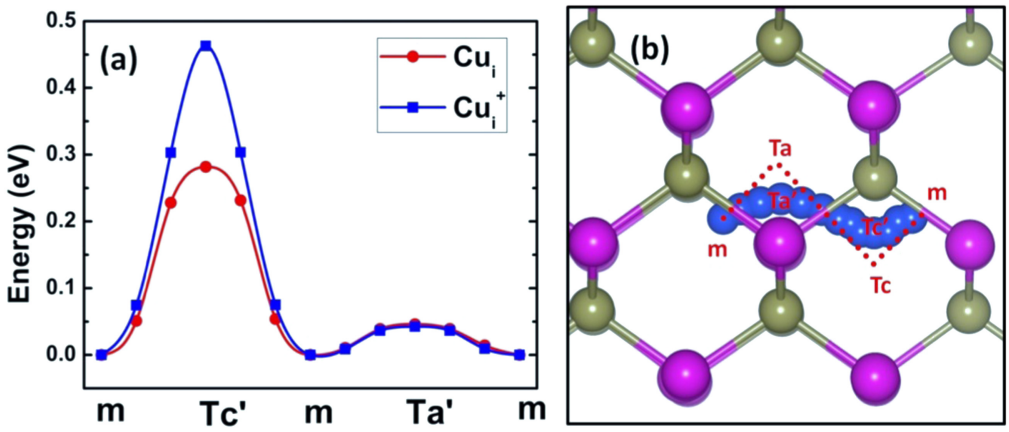

Figure 18. (a) Diffusion energies and (b) diffusion paths of Cu interstitial. The pink balls are Cd atoms, the brown balls are Te atoms, and the blue balls are Cu atoms.

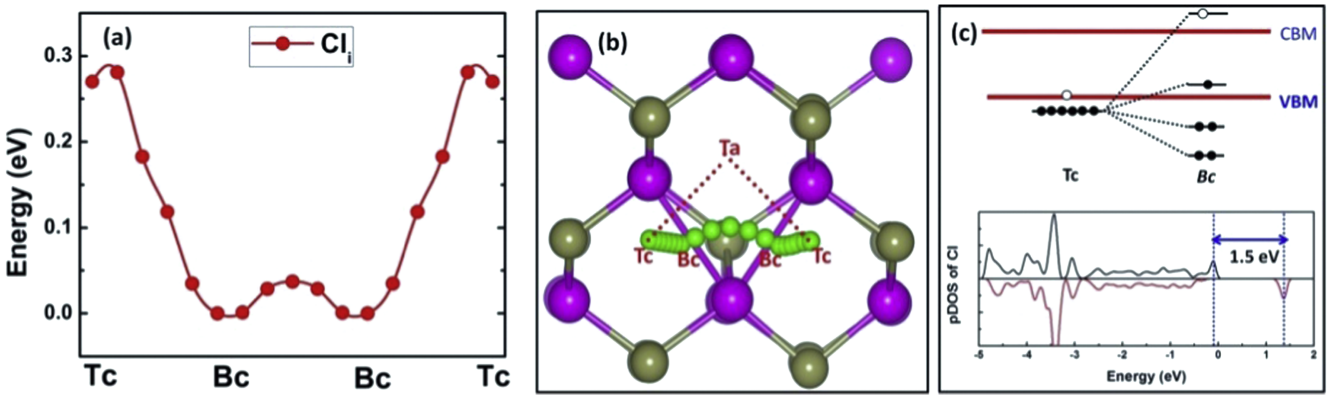

Figure 19. (a) Diffusion energies and (b) diffusion paths of neutral Cl interstitial. The pink balls are Cd atoms, the brown balls are Te atoms, and the green balls are Cl atoms. (c) The diagrams to show the electron occupations of the T_c and B_c sites and partial density of state of Cl interstitial at the B_c sites, where a large spin-splitting energy of 1.5 eV is clearly seen.

be 0.28 eV by HSE06, which is larger than the PBE results (0.1 eV in [51]). Negatively charged Cl_i^- is most stable at the T_c site, mainly determined by the strong Coulomb attractions between Cl_i^- and the neighboring four cations. Because all the orbitals of Cl_i^- are fully occupied, no level splitting is observed and Cl_i^- follows the common diffusion paths with a diffusion energy barrier of 0.89 eV, as shown in figures 20(a) and (b). Positively charged Cl_i^+, on the other hand, is most stable at the *Spl* site due to the level splitting, as already discussed in section 4 and shown in figure 11. In this case,

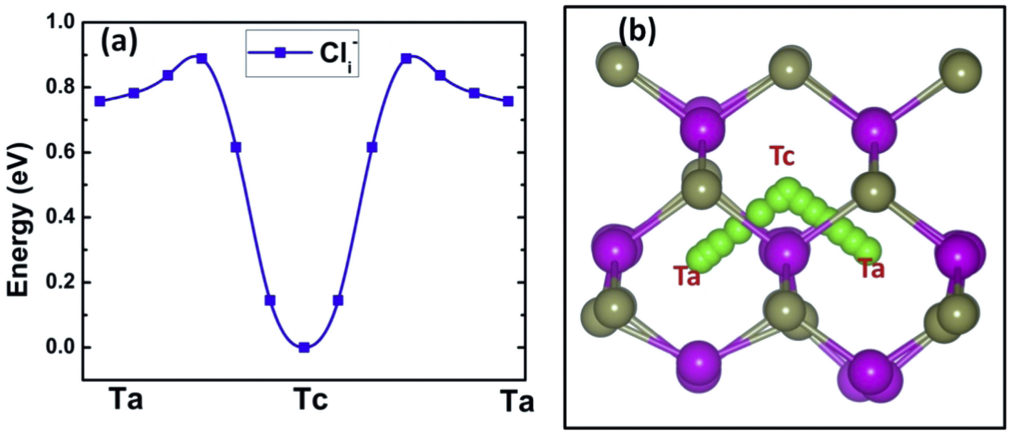

Figure 20. (a) Diffusion energies and (b) diffusion paths of negatively charged Cl interstitial. The pink balls are Cd atoms, the brown balls are Te atoms, and the green balls are Cl atoms.

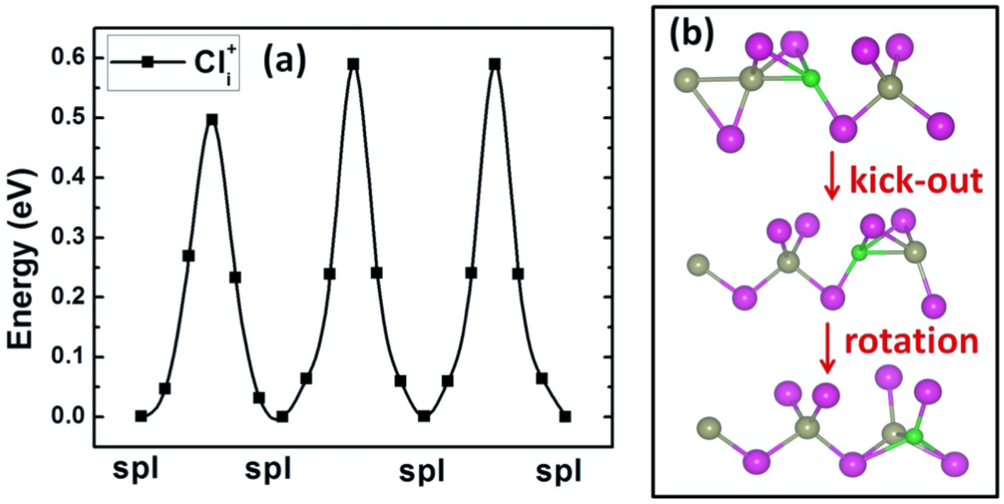

Figure 21. (a) Diffusion energies and (b) diffusion paths of positively charged Cl interstitial. The pink balls are Cd atoms, the brown balls are Te atoms, and the green balls are Cl atoms.

Cl_i^+ diffuses differently from its neutral and negatively charged states. At the first step, the Te atom initially bonded to the Cl atom kicks the Cl forward and itself becomes a normal, four-cation bonded anion, while the Cl forms a new bond with another Te atom and they share the original site of this Te, as shown in figure 21(b). Then this Cl–Te bond rotates by about 90° and followed by another equivalent rotation, the Cl–Te bond finally becomes a Te–Cl bond, which is equivalent to the initial structure. By combining one kick-out step and two rotation steps, Cl_i^+ has a relatively low energy barrier of about 0.6 eV, as shown in figure 21(a).

P interstitial can also have three charge states. Both neutral and negatively charged P interstitials are most stable at the *Spl* site, the same as for the positively charged Cl_i^+. Consequently, their diffusion mechanisms are also the same as those of Cl_i^+, i.e. first a kick-out step, then followed by two rotation steps. Due to the stronger bonding between P and Te, neutral and negatively charged P interstitial have their largest energy barriers at the kick-out steps with values of 0.4 and 0.85 eV, respectively, as shown in figure 22. Positively charged P_i^+ has a different energy minimum, which locates at the center of the six-atom rings formed by Cd and Te atoms (denoted as *C* site), as shown in figure 23(b). At the *C* site, there can be large energy gain due to level splitting, as seen in figure 23(c). Consequently, the diffusion of positively charged P interstitial has an energy barrier of about 0.6 eV, as shown in figure 23(a).

In this section, we established the correlation between the diffusion behavior and the electronic structure of the interstitial diffuser. For the cation atoms, because the defect electrons occupy the non-degenerate *s*-like state under T_d symmetry, the diffusion is almost along the [109] directions between the tetrahedral sites, although the diffusion of Cu shows some deviation due to the *s*–*d* coupling. The diffusion of the neutral and positively charged cation atoms follows similar paths. For the anion atoms, because the defect electrons occupy the *p*-like triply-degenerate states under T_d symmetry, there are always large structural distortions. Therefore, the diffusion follows totally different paths, and strongly depends on the charge states of the interstitial diffusers.

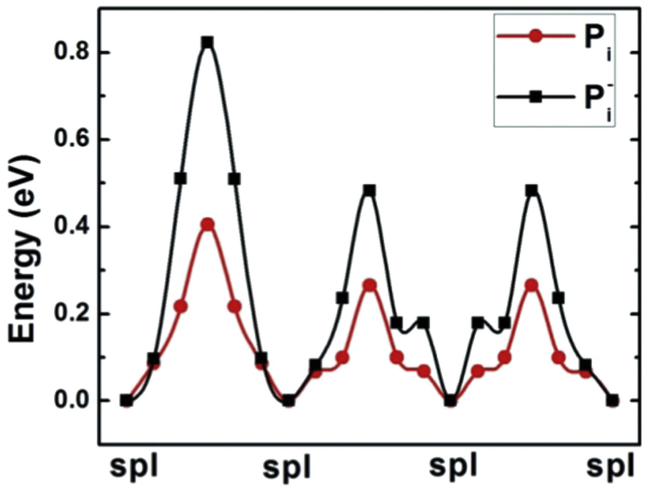

Figure 22. Diffusion energies of neutral and negatively charged P interstitials.

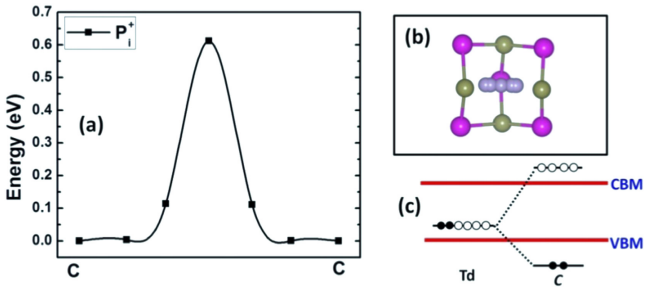

Figure 23. (a) Diffusion energies and (b) diffusion paths of positively charged P interstitial. The pink balls are Cd atoms, the brown balls are Te atoms, and the light purple balls are P atoms. (c) The diagram to shows the electron occupations of positively charged P interstitials at the *C* sites.

Here, we also want to stress that we just considered the simplest interstitial diffusion of Na, Cu, Cl, and P. Although this information can help with understanding impurity behaviors and controlling their incorporation and device performance, direct comparisons between our calculations and experiments can have gaps because, in reality, other diffusion mechanisms can coexist with the ones studied in this work. In addition, impurities like Cu, Cl, and P usually have large amounts in CdTe and they can form many defect complexes like donor–acceptor pairs, which can significantly affect their diffusion as well as the device stability. These issues need to be addressed to fully understand the impurity behaviors in CdTe.

7. Conclusion and outlook

We summarize the recent first-principles study of defects in CdTe as follows: (1) Intrinsic CdTe can only be poorly *p*-type and have a hole density less than 10^{15} cm^{-3} due to the relatively deep acceptor level of V_{Cd}. Homo CdTe *p*-n junction could give high V_{oc} as long as the surface recombination can be suppressed. (2) The dominant defect recombination center in *p*-type bulk CdTe is Te_{Cd}^{2+}, which limits carrier lifetime to be around 200 ns. (3) *P*-type doping by replacing Te with group V elements generally will be limited by their AX centers, which can be overcome through a non-equilibrium thermal rapid-cooling process. The hole density can be improved to be over 10^{17} cm^{-3}. However, the long-term stability will be a challenging issue. (4) Although *p*-type doping by replacing Cd with group I alkaline elements is also limited by compensated alkaline interstitials, the non-equilibrium thermal rapid-cooling process has proved to be efficient in enhancing the hole density to the order of 10^{17} cm^{-3}. (5) Cu can improve *p*-type doping, but Cl is found to be unsuitable for this. Both Cu and Cl show segregation at GBs, especially at those with Te–Te wrong bonds. (6) External impurity diffusion in CdTe is strongly correlated with the impurity electronic structures, especially for anion diffusion.

Although first-principles calculations have already provided much knowledge of defect behaviors in CdTe and helped us understand important issues related to the efficiency and stability of CdTe solar cells, much more is still to be explored, including but not limited to the following. (1) What are the defect properties at CdTe surfaces and interfaces? Can new architectures such as those based on homo CdTe *p*-n junctions with surfaces passivated by MnCdTe or MgCdTe alloys give us higher energy conversion efficiency? (2) How can we improve the stability of group VA and group IA elements doped *p*-type CdTe using strain or co-doping strategies? (3) In considering the large number of defect complexes or donor–acceptor pairs in CdTe, how do they affect the performance of CdTe solar cells in terms of doping, recombination, and diffusion, as well as the stability of device performance? (4) Although Cu is critical to obtain high efficiency, how can we improve the stability? Can we find better substitutions of Cu-containing back contacts? (5) CdS window layer is also important for current CdTe solar cells. Can we improve the band alignments at CdTe/CdS interfaces and reduce the interface recombination through alloying? We believe first-principles calculations of defect behaviors in CdTe can continue to give us valuable information in the future.

Acknowledgments

We would like to thank T Barnes, W Metzger, D Vasileska, I Sankin, D Kuciauskas, J Li, Y Yan, J Sites, K Lynn and S Seyedmohommadi for valuable discussions. The work at NREL was funded by the US Department of Energy under Contract No. DE-AC36-08GO28308. The calculations were done on NREL's Peregrine supercomputer and at the National Energy Research Scientific Computing Center, which is supported by the Office of Science of the US Department of Energy under Contract No. DE-AC02-05CH11231.

References

[1] Loferski J J 1956 *J. Appl. Phys.* **27** 777
[2] Zanio N 1978 Cadmium telluride *Semiconductors and Semimetals* vol 13 ed R K Willardson and A C Beer (New York: Wiley)

[3] Durose K, Edwards P R and Halliday D P 1999 *J. Cryst. Growth* **197** 733
[4] Mitchell K W, Fahrenbruch A L and Bube R H 1977 *J. Appl. Phys.* **48** 4365
[5] Chu T L, Chu S S, Ferekides C, Wu C Q, Britt J and Wang C 1991 *J. Appl. Phys.* **70** 7608
[6] Chu T L and Chu S S 1995 *Solid-State Electron.* **38** 533
[7] Razykov T M, Ferekides C S, Morel D, Stefanakos E, Ullal H S and Upadhyaya H M 2011 *Sol. Energy* **85** 1580
[8] Wu X 2004 *Sol. Energy* **77** 803
[9] Romeo N, Bosio A, Canevari V and Podestà A 2004 *Sol. Energy* **77** 795
[10] Ferekides C S, Marinskiy D, Viswanathan V, Tetali B, Palekis V, Selvaraj P and Morel D L 2000 *Thin Solid Films* **361** 520
[11] Kazmerski L L 2006 *J. Electron. Spectrosc. Relat. Phenom.* **150** 105
[12] Dobson K D, Visoly-Fisher I, Hodes G and Rose D 2000 *Sol. Energy Mater. Sol. Cells* **62** 295
[13] Britt J and Ferekides C 1993 *Appl. Phys. Lett.* **62** 2851
[14] Chopra K L, Paulson P D and Dutta V 2004 *Prog. Photovolt: Res. Appl.* **12** 69
[15] Bonnet D and Meyers P 1998 *J. Mater. Res.* **13** 2740
[16] Best Research-Cell Efficiencies, National Renewable Energy Laboratory (http://nrel.gov/ncpv/images/efficiency_chart.jpg) (accessed April 6th, 2016)
[17] Sites J and Pan J 2007 *Thin Solid Films* **515** 6099
[18] Kanevce A and Gessert T A 2011 *IEEE J. Photovoltaics* **1** 99
[19] Mahabaduge H P *et al* 2015 *Appl. Phys. Lett.* **106** 133501
[20] Dzhafarov T D, Yesilkaya S S, Canlia N Y and Caliskan M 2005 *Sol. Energy Mater. Sol. Cells* **85** 371
[21] Grecu D, Compaan A D, Young D, Jayamaha U and Rose D H 2000 *J. Appl. Phys.* **88** 2490
[22] Bätzner D L, Romeo A, Terheggen M, Döbeli M, Zogga H and Tiwaria A N 2004 *Thin Solid Films* **451** 536
[23] Berding M A 1999 *Appl. Phys. Lett.* **74** 552
[24] Meyer B K and Stadler W 1996 *J. Cryst. Growth* **161** 119
[25] Hofmann D M, Stadler W, Christmann P and Meyer B K 1996 *Nucl. Instrum. Methods Phys. Res., Sect.* A **380** 117
[26] Soundararajan R, Lynn K G, Awadallah S, Szeles C and Wei S-H 2006 *J. Electron. Mater.* **35** 1333
[27] McCandless B E, Moulton L V and Birkmire R W 1997 *Prog. Photovolt: Res. Appl.* **5** 249
[28] Molva E, Pautrat J L, Saminadayar K, Milchberg G and Magnea N 1984 *Phys. Rev.* B **30** 3344
[29] Francou J M, Saminadayar K and Pautrat J L 1990 *Phys. Rev.* B **41** 12035
[30] Hofmann D M, Omling P, Grimmeiss H G, Meyer B K, Benz K W and Sinerius D 1992 *Phys. Rev.* B **45** 6247
[31] Emanuelsson P, Omling P, Meyer B K, Wienecke M and Schenk M 1993 *Phys. Rev.* B **47** 15578
[32] Berding M A 1999 *Phys. Rev.* B **60** 8943
[33] Wei S-H and Zhang S B 2002 *Phys. Rev.* B **66** 155211
[34] Chang Y-C, James R B and Davenport J W 2006 *Phys. Rev.* B **73** 035211
[35] Du M-H, Takenaka H and Singh D J 2008 *Phys. Rev.* B **77** 094122
[36] Carvalho A, Tagantsev A K, Öberg S, Briddon P R and Setter N 2010 *Phys. Rev.* B **81** 075215
[37] Zhang L, Da Silva J L F, Li J, Yan Y, Gessert T A and Wei S-H 2008 *Phys. Rev. Lett.* **101** 155501
[38] Krasikov D, Knizhnik A, Potapkin B and Sommerer T 2013 *Semicond. Sci. Technol.* **28** 125019
[39] Krasikov D, Knizhnik A, Potapkin B, Selezneva S and Sommerer T 2013 *Thin Solid Films* **535** 322
[40] Major J D, Treharne R E, Phillips L J and Durose K 2014 *Nature* **511** 334
[41] Du M-H, Takenaka H and Singh D J 2008 *J. Appl. Phys.* **104** 093521
[42] Lordi V 2013 *J. Cryst. Growth* **379** 84
[43] Biswas K and Du M-H 2012 *New J. Phys.* **14** 063020
[44] Lindström A, Mirbt S, Sanyal B and Klintenberg M 2016 *J. Phys. D: Appl. Phys.* **49** 035101
[45] Shepidchenko A, Sanyal B, Klintenberg M and Mirbt S 2015 *Sci. Rep.* **5** 14509
[46] Castaldini A, Cavallini A, Fraboni B, Fernandez P and Piqueras J 1998 *J. Appl. Phys.* **83** 2121
[47] Szeles C, Shan Y, Lynn K, Moodenbaugh A and Eissler E 1997 *Phys. Rev.* B **55** 6945
[48] Reislöhner U, Grillenberger J and Witthuhn W 1998 *J. Cryst. Growth* **184** 1160
[49] Krsmanovic N, Lynn K G, Weber M H, Tjossem R, Gessmann T, Szeles C, Eissler E E, Flint J P and Glass H L 2000 *Phys. Rev.* B **62** 16279
[50] Ma J, Kuciauskas D, Albin D, Bhattacharya R, Reese M, Barnes T, Li J V, Gessert T and Wei S-H 2013 *Phys. Rev. Lett.* **111** 067402
[51] Ma J, Yang J, Wei S-H and Da Silva J L F 2014 *Phys. Rev.* B **90** 155208
[52] Yang J-H, Yin W-J, Park J-S, Burst J, Metzger W K, Gessert T, Barnes T and Wei S-H 2015 *J. Appl. Phys.* **118** 025102
[53] Yang J-H, Park J-S, Kang J and Wei S-H 2015 *Phys. Rev.* B **91** 075202
[54] Yang J-H, Park J-S, Kang J, Metzger W, Barnes T and Wei S-H 2014 *Phys. Rev.* B **90** 245202
[55] Park J-S, Kang J, Yang J-H, Metzger W and Wei S-H 2015 *New J. Phys.* **17** 013027
[56] Yang J-H, Shi L, Wang L-W and Wei S-H 2016 *Sci. Rep.* **6** 21712
[57] Yang J-H, Yin W-J, Park J-S and Wei S-H 2016 *J. Appl. Phys.* **119** 045104
[58] Hohenberg P and Kohn W 1964 *Phys. Rev.* **136** B864
[59] Kohn W and Sham L J 1965 *Phys. Rev.* **140** A1133
[60] Kresse G and Furthmüller J 1996 *Phys. Rev.* B **54** 11169
[61] Kresse G and Furthmüller J 1996 *Comp. Mater. Sci.* **6** 15
[62] Kresse G and Joubert D 1999 *Phys. Rev.* B **59** 1758
[63] Heyd J, Scuseria G E and Ernzerhof M 2003 *J. Chem. Phys.* **118** 8207
[64] Perdew J P, Burke K and Ernzerhof M 1996 *Phys. Rev. Lett.* **77** 3865
[65] Wei S-H 2004 *Comp. Mater. Sci.* **30** 337
[66] Yang J-H, Chen S, Xiang H and Gong X G 2011 *Phys. Rev.* B **83** 235208
[67] Yin W-J, Ma J, Wei S-H, Al-Jassim M M and Yan Y 2012 *Phys. Rev.* B **86** 045211
[68] Sze S 1981 *Physics of Semiconductor Devices* 2nd edn (New York: Wiley)
[69] Ma J, Wei S-H, Gessert T A and Chin K K 2011 *Phys. Rev.* B **83** 245207
[70] Romestain R and Weisbuch C 1980 *Phys. Rev. Lett.* **45** 2067
[71] Shi L and Wang L-W 2012 *Phys. Rev. Lett.* **109** 245501
[72] Shi L, Xu K and Wang L-W 2015 *Phys. Rev.* B **91** 205315
[73] Pässler R 1974 *Czech. J. Phys.* B **24** 322
[74] Pässler R 1982 *Czech. J. Phys.* B **32** 846
[75] Mills G, Jónsson H and Schenter G K 1995 *Surf. Sci.* **324** 305
[76] Vineyard G H 1957 *J. Phys. Chem. Solids* **3** 121
[77] Tsuchiya T 2011 *Appl. Phys. Express* **4** 094104
[78] Reshchikov M A *et al* 2011 *Phys. Rev.* B **84** 075212
[79] Jursenas S, Miasojedovas S, Kurilcik G, Zukauskas A and Hageman P R 2003 *Appl. Phys. Lett.* **83** 66
[80] Nelson J 2003 *The Physics of Solar Cells* (London: Imperial College)
[81] Kuciauskas D, Kanevce A, Dippo P, Seyedmohammadi S and Malik R 2015 *IEEE J. Photovolt.* **5** 366
[82] Park J H, Farrell S, Kodama R, Blissett C, Wang X, Colegrove E, Metzger W K, Gessert T A and Sivananthan S 2014 *J. Electron. Mater.* **43** 2998

[83] Fanrenbruch A 1987 *Sol. Cells* **21** 399
[84] Morehead F F and Mandel G 1964 *Phys. Lett.* **10** 5
[85] Selim F A and Kröger F A 1977 *J. Electrochem. Soc.* **124** 401
[86] Anthony T C, Fahrenbruch A L, Peters M G and Bube R H 1985 *J. Appl. Phys.* **57** 400
[87] Zandian M, Chen A C, Edwall D D, Pasko J G and Arias J M 1997 *Appl. Phys. Lett.* **71** 2815
[88] Hails J E, Irvine S J C, Cole-Hamilton D J, Giess J, Houlton M R and Graham A 2008 *J. Electron. Mater.* **37** 1291
[89] Arias J M, Shin S H, Cooper D E, Zandian M, Pasko J G, Gertner E R, DeWames R E and Singh J 1990 *J. Vac. Sci. Technol.* **A8** 1025
[90] Kraft C, Brömel A, Schönherr S, Hädrich M, Reislöhner U, Schley P, Gobsch G, Goldhahn R, Wesch W and Metzner H 2011 *Thin Solid Films* **519** 7153
[91] Park C H and Chadi D J 1995 *Phys. Rev. Lett.* **75** 1134
[92] Chadi D J 1999 *Phys. Rev.* B **59** 15181
[93] Duenow J N, Burst J M, Albin D S, Kuciauskas D, Johnston S W, Reedy R C and Metzger W K 2014 *Appl. Phys. Lett.,* **105** 053903
[94] Crowder B L and Hammer W N 1966 *Phys. Rev.* **150** 541
[95] Altosaara M, Kukkb P-E and Mellikov E 2000 *Thin Solid Films* **361** 443
[96] Burst J M *et al* 2016 *Nature Energy* **1** 16015
[97] Moutinho H R, Al-Jassim M M, Levi D H, Dippo P C and Kazmerski L L 1998 *J. Vac. Sci. Technol.* **A16** 1251
[98] Metzger W K, Albin D, Romero M J, Dippo P and Young M 2006 *J. Appl. Phys.* **99** 103703
[99] Terheggen M, Heinrich H, Kostorz G, Romeo A, Baetzner D, Tiwari A N, Bosio A and Romeo N 2003 *Thin Solid Films* **431** 262
[100] Komin V, Tetali B, Viswanathan V, Yu S, Morel D L and Ferekides C S 2003 *Thin Solid Films* **431** 143
[101] Ringel S A, Smith A W, MacDougal M H and Rohatgi A 1991 *J. Appl. Phys.* **70** 881
[102] Visoly-Fisher I, Cohen S R, Gartsman K, Ruzin A and Cahen D 2006 *Adv. Funct. Mater.* **16** 649
[103] Visoly-Fisher I, Cohen S R, Ruzin A and Cahen D 2004 *Adv. Mater.* **16** 879
[104] Li C *et al* 2014 *Phys. Rev. Lett.* **112** 156103
[105] Rose D H, Hasoon F S, Dhere R G, Albin D S, Ribelin R M, Li X S, Mahathongdy Y, Gessert T A and Sheldon P 1999 *Prog. Photovolt: Res. Appl.* **7** 331
[106] Adirovich E I, Yuabov Y M and Yagudaev G R 1969 *Sov. Phys.: Semicond.* **3** 61
[107] Kranz L *et al* 2013 *Nature Commun.* **4** 2306
[108] Perrenoud J, Kranz L, Gretener C, Pianezzi F, Nishiwaki S, Buecheler S and Tiwari A N 2013 *J. Appl. Phys.* **114** 174505
[109] Yan Y, Al-Jassim M M and Wei S-H 2006 *Appl. Phys. Lett.* **89** 181912
[110] Balcioglu A, Ahrenkiel R K and Hasoon F 2000 *J. Appl. Phys.* **88** 7175
[111] Gippius A A, Panossian J R and Chapnin V A 1974 *Phys. Status Solidi* **A21** 753
[112] Kröger F A 1977 *Rev. Phys. Appl. (Paris)* **12** 205
[113] Gilmore A S, Kaydanov V and Ohno T R 2003 *Mater. Res. Soc.* **763** B9.6
[114] Chamonal J P, Molva E and Pautrat J L 1982 *Solid State Commun.* **43** 801
[115] Said M and Kanehisa M A 1990 *J. Cryst. Growth* **101** 488
[116] Ma J and Wei S-H 2013 *Phys. Rev. Lett.* **110** 235901
[117] Jones E D, Stewart N M and Mullin J B 1992 *J. Cryst. Growth* **117** 244
[118] Woodbury H H and Aven M 1968 *J. Appl. Phys.* **39** 5485
[119] Baetzner D L, Romeo A, Zogg H, Wendt R and Tiwari A N 2001 *Thin Solid Films* **387** 151
[120] Yan Y, Al-Jassim M M, Jones K M, Wei S-H and Zhang S B 2000 *Appl. Phys. Lett.* **77** 1461
[121] Yan Y, Al-Jassim M M and Jones K M 2003 *J. Appl. Phys.* **94** 2976
[122] Sun C, Lu N, Wang J, Lee J, Peng X, Klie R F and Kim M J 2013 *Appl. Phys. Lett.* **103** 252104